DEVELOPMENT OF LATERAL MIGRATION BACKSCATTER RADIOGRAPHY AND ASSOCIATED IMAGE ENHANCEMENT ALGORITHMS

By

SHYAM PRASAD KESHAVMURTHY

A DISSERTATION PRESENTED TO THE GRADUATE SCHOOL
OF THE UNIVERSITY OF FLORIDA IN PARTIAL FULFILLMENT
OF THE REQUIREMENTS FOR THE DEGREE OF
DOCTOR OF PHILOSOPHY

UNIVERSITY OF FLORIDA

1996

This dissertation is dedicated to my parents Mr. and Mrs. Keshavmurthy.

ACKNOWLEDGMENTS

The author expresses his appreciation for the guidance, motivation, criticism, encouragement and financial support provided by his academic advisor, Dr. Edward T. Dugan. His enthusiasm and constant support provided a great impetus for conducting this research work. The author is grateful for the support and encouragement provided by Dr. Alan Jacobs, during this research work. His criticisms helped the author to get better perspective of the landmine detection problem. The technical advice provided by Dr. Andrew Laine were invaluable. His encouragement and advice helped the author in developing the image enhancement algorithm presented in this dissertation. The author thanks Dr. Nils Diaz for the advice regarding experimental work and providing access to the computer facilities at INSPI for this research work. The author thanks Dr. Joseph Glover for his encouragement, criticism and advice regarding the validity of Monte Carlo method of simulation. The author also thanks Dr. Samim Anghaie for providing the photon cross-section data and for his advice regarding other methods of scatter radiography.

The author expresses special thanks to his friend and colleague Mr. Joseph Wehlburg for providing technical and nontechnical support during this research. The author expresses his appreciation to the staff in the Nuclear Engineering Sciences Department for providing timely nontechnical support during this research.

The author thanks the U.S. Army CECOM Night Vision and Electronic Sensor Directorate for providing financial support for conducting this research.

TABLE OF CONTENTS

ACKNOWLEDGMENTS iv

LIST OF TABLES viii

LIST OF FIGURES ix

ABSTRACT xiii

CHAPTERS

1 INTRODUCTION 1

2 OVERVIEW OF SCATTER RADIOGRAPHY 5
  COMSCAN 7
  Coherent X-ray Scatter Tomography 9
  COMTEL 11
  Dynamic Radiography 12
  Compton Profilometry 12
  Lateral Migration Backscatter Radiography (LMBR) 13

3 MONTE CARLO METHOD FOR PHOTON TRANSPORT SIMULATION 16
  Mechanics of MC Method for Photon Transport Simulation 17
  Verification of the Suitability of the MCNP
  Random Number Generator for Solving Particle Transport Problems 21
  Validation of the MCNP Results Against Measurements
  for a Photon Transport Problem 29

4 ANALYSIS OF PHOTON TRANSPORT IN A LMBR SYSTEM 45
  Analysis of Scatter Components in LMBR system 46
  Verification of MCNP-SABRINA Results with
  Analytical Calculations 49
  Detector Design for LMBR Landmine Detection System 52
  Features in LMBR Images 58

5 X-RAY SOURCE SPECTRA SIMULATION (XSPEC) 68
  Computer Program XSPEC 71
  Calculation of Bremsstrahlung Spectra 71
  Characteristic Spectra Calculation 72
  Measurement of Maxitron X-ray Spectra 73
  Monte Carlo Simulation of X-ray Source 76
  Results and Discussion 77

6 APPROXIMATE SOLUTIONS TO THE LATERAL MIGRATION BACKSCATTER (LMB)
  PHOTON TRANSPORT 83
  Two-collision Model for LMB Photon Transport 83
  LMBR Image Restoration 88
  Specialized Monte Carlo Model, Photon Lateral
  Migration Simulator(PLMS) 90
  Detector model in PLMS 96

7 LMER IMAGE ENHANCEMENT ALGORITHMS 102
  Introduction 103
  Background 105
  Implementation 106
  Comparison of AoW Approximation with Other
  Interpolation Methods 117
  Application to Landmine Detection 120
  Application to Mammography 123
  Summary 124

8 SUMMARY AND CONCLUSIONS 127
  Future developments 132

APPENDICES

A THE MONTE CARLO SOLUTION TO THE BOLTZMANN TRANSPORT EQUATION 135

B CALCULATION OF AVERAGE ENERGY AND ANGLES FOR COMPTON SCATTER 138

C XSPEC: THE X-RAY SPECTRA SIMULATION PROGRAM 140

D THE PROGRAM PLMS 145

LIST OF REFERENCES 153

BIOGRAPHICAL SKETCH 156

LIST OF TABLES

Table Page

3-1 The number of pseudo-random numbers used for a typical MCNP simulation 24

3-2 Source strength comparison between MCNP and the Maxitron measurements 28

4-1 The average scattering angles and energies of first-scattered photons 50

4-2 Average scattering angles of the scattering components relative to the incident x-ray beam direction 52

4-3 Effect of length of the first collimator on the collimated detector performance 55

4-4 Effect of raster gap size on the uncollimated detector performance 55

4-5 The design parameters for an optimized detector with a symmetric source position and detector height of 30 cm above the ground 58

4-6 The summary of LMBR image features 65

5-1 The fractional yield values used in XSPEC for calculating characteristic spectra 73

5-2 Filters used for spectra measurement 74

5-3 Comparison of shape indices for the Maxitron x-ray generator predicted and measured spectra 78

6-1 The mine parameter predictions of the original two-collision model 86

6-2 Predicted mine parameters with the modified two-collision model 88

6-3 The comparison of the mine parameter predictions by the modified two-collision model with the predictions by the original model for the test image 90

6-3 The energy of an equivalent monoenergetic source 95

LIST OF FIGURES

Figure page

2-1 Comparison of scattering probabilities of three materials . . . 8

2-2 Scatter imaging applications. (a)COMSCAN (b)X-ray scatter tomography (c) COMTEL (d)dynamic radiography (e)Compton profile . . . 13

2-3 Schematic of the LMBR landmine imaging system . . . 14

3-1 Flow chart for Monte Carlo simulation of photon transport . . . 18

3-2 Monte Carlo Scheme for calculating the scattering angle and energy of a photon . . . 19

3-3 Monte Carlo scheme for calculating direction cosines and coordinates after each collision . . . 20

3-4 Monte Carlo scheme for determining the interacting material . . . 22

3-5a Setup of Maxitron x-ray generator used in MCNP electron-photon transport simulation . . . 25

3-5b The voltage and the current wave form used in MCNP electron source simulation . . . 25

3-6 Experimental setup used for x-ray source strength measurement . . . 27

3-7 MCNP simulation of the photon transport in the landmine imaging system . . . 28

3-8 Measurement setup used for MCNP validation . . . 30

3-9 X-ray spectrum used for MCNP photon transport validation . . . 33

3-10 The MCNP generated collimated detector image of a 12 inch diameter plastic landmine buried at (17,17) and 1 inch DOB . . . 34

3-11 The measured collimated detector image of a 12 inch diameter plastic landmine buried at (18,18) and 1 inch DOB . . . 35

3-12 The MCNP generated uncollimated detector image of a 12 inch diameter plastic landmine buried at (17,17) and 1 inch DOB . . . 36

3-13 The measured uncollimated detector image of a 12 inch diameter plastic landmine buried at (16,16) and 1 inch DOB . . . 37

3-14 Single scan-line results of MCNP compared with measurements for 1/2 inch per foot slope in the motion direction 40

3-15 Single scan-line results of MCNP compared with measurements for 1/2 inch per foot slope in the center direction 40

3-16 Single scan-line results of MCNP compared with measurements for 1 inch per foot slope in the motion direction 42

3-17 Single scan-line results of MCNP compared with measurements for 1 inch per foot slope in the center direction 42

3-18 Comparison of MCNP single scan-line results with measurements for a 12 inch diameter plastic mine buried at 1 inch DOB with 1/2" per foot soil slope in motion direction 44

3-19 Comparison of MCNP single scan-line results with measurements for a 12 inch diameter plastic mine buried at 1 inch DOB with 1/2" per foot soil slope in motion direction 44

4-1 The first-collision components for a collimated detector a) all first-collision components b) first-collision components from mine 47

4-2 The collision components from mine a) second-collision b) third-collision c) fourth-collision 48

4-3 The average scattering energy for the first scatter photons 51

4-4 The average scattering angle for the first-scatter photons 51

4-5 Schematic representation of collision component paths using average scattering angles 53

4-6 Effect of collimator length on the collision components (a) first-collision component (b) second-collision component (c) third-collision component 57

4-7 MCNP generated images from front collimated detector a) 12 inch diameter all plastic mine located at (17,17) and 1 inch DOB (b) 12 inch diameter plastic mine with metal casing at (0,0) and 1 inch DOB, (c) a 12 inch diameter pot-hole 1 inch deep at (0,9) 60

4-8 MCNP generated images from front uncollimated detector a) 12 inch diameter all plastic mine located at (17,17) and 1 inch DOB (b) 12 inch diameter plastic mine with metal casing at (0,0) and 1 inch DOB, (c) a 12 inch diameter pot-hole 1 inch deep at (0,9) 61

4-9 Schematic representation to demonstrate the reason for the peak shift in LMBR images 62

4-10 Measured images from front collimated detector (a) 12 inch diameter plastic mine with metal casing at (0,0) and 1 inch DOB, (b) a 12 inch diameter pot-hole 1 inch deep at (0,0) 66

4-11 Measured images from front uncollimated detector (a) 12 inch diameter plastic mine with metal casing at (9,9) and 1 inch DOB, (b) a 12 inch diameter pot-hole 1 inch deep at (9,9) 67

5-1 Comparison of experimental and computed bremsstrahlung spectra generated at 140 kVcp from Tucker et al.[19] 70

5-2 Comparison of tungsten spectra for a tungsten target at 20° angle and 2.7mm Al filtration from Tan and Heaton [17] 70

5-3 Schematic of the detection system used for x-ray spectra measurements 75

5-4 Comparison of XSPEC, MCNP and measured Maxitron x-ray spectra at 100 kVp 81

5-5 Comparison of XSPEC, MCNP and measured Maxitron x-ray spectra at 150 kVp 81

5-6 Comparison of XSPEC, MCNP and measured Maxitron x-ray spectra at 175 kVp 82

5-7 Comparison of XSPEC, MCNP and measured Maxitron x-ray spectra at 200 kVp 82

6-1 Schematics illustrating the notations used in the two-collision models 85

6-2 Image used for testing the modified two-collision model 92

6-3 Restored image using modified two-collision model 95

6-4 Restored image using the original two-collision model 99

6-5 FIMS generated images for the front collimated detector 99

6-6 Measured front collimated detector image of a 12" diameter plastic landmine at (25,25). 12" diameter metal mine at (10,10), and a 3" diameter metal landmine at (4,27) 100

6-5 The single scan-line results from FIMS for 1/2" per foot soil slope 101

7-1 The synthetic image used for testing AoW algorithm 107

7-2 One-dimensional AoW filters in Fourier domain 108

7-3 The two-dimensional AoW filters in Fourier domain 110

7-4 The AoW filter coefficients of the synthetic image from Figure 7-1 111

7-5 The log-log plot of filter coefficients versus scale. scale is presented in powers of two 112

7-6 Comparison of estimated level L7 filter coefficients with respect to the actual AnW shell level L7 filter coefficients for the synthetic image . . . 113

7-7 The schematic of the AnW algorithm . . . 115

7-8 Enlarged synthetic image from Figure 7-1 . . . 116

7-9 Comparison of the sub-sampled and then extrapolated Lenna image with the original . . . 118

7-10 Comparison of image interpolation algorithms . . . 119

7-11 The simulated mine field image . . . 121

7-12 The zero-crossing representation of the AnW filter coefficients of a simulated mine-field image . . . 122

7-13 The M-19 mine and typical cylindrical mines . . . 122

7-14 The sub-pixel expanded (6X) mine-field image . . . 123

7-16 The under-sampled mammogram . . . 125

7-17 The comparison of the extrapolated image with the original mammogram along with a comparison of a region of interest . . . 126

Abstract of Dissertation Presented to the Graduate School
of the University of Florida in Partial Fulfillment of the
Requirements for the Degree of Doctor of Philosophy

DEVELOPMENT OF LATERAL MIGRATION BACKSCATTER RADIOGRAPHY AND ASSOCIATED IMAGE ENHANCEMENT ALGORITHMS

By

Shyam Prasad Keshavmurthy

August 1996

Chairman: Edward T. Dugan
Major Department: Nuclear Engineering Sciences

X-ray scattering in any medium produces multiple-collision photons, these photons are often treated as noise when used for imaging purposes. Most imaging modilities that use scattered radiation to generate images use only the first-scatter photons and employ detector collimators to minimize the contribution of multiple-scattered photons. The reliance on first-scattered photons by scatter radiography systems can put a huge demand on the x-ray source strength requirement and often these systems need elaborate image reconstruction algorithms to get meaningful information. This reliance on first-scatter also restricts their application to situations wherein the imaged surfaces are smooth or pre-defined.

To make use of the multiple collision photons, this dissertation develops the theory of *lateral migration backscatter radiography* (LMBR). This imaging modality uses two pairs of large area detectors. Each set has a detector that is collimated to image predominantly

multiple-scattered photons and the other uncollimated to predominantly image first-scatter photons. This allows generation of two separate images, one containing surface features and the other containing both surface and subsurface features. These two images make LMBR useful for imaging objects with unknown surface imperfections. The use of large area detectors also reduces the requirement of very high x-ray source strength for scatter x-ray radiography.

The principles of LMBR are demonstrated through Monte Carlo simulation of photon transport. The Monte Carlo results are presented both quantitatively and graphically. The Monte Carlo simulation results are also verified with measurements from a LMBR system used for landmine detection.

On the basis of the detailed Monte Carlo analysis of LMBR systems, two approximate solutions to photon transport in the LMBR systems have been developed. The first approach approximates the solution by treating the LMBR image formation as a pseudo-inverse problem, and the second method approximates the photon transport through a specialized Monte Carlo scheme. The results from these two solution methods are compared with measured results.

The LMBR system used for landmine detection produces low-resolution under sampled images; additionally, region of interest images extracted from an original image may make more obvious sampling artifacts. Low-resolution images can broadly be classified as under sampled images. Wavelet based multi-resolution analyses are less effective on such under sampled images because the sub-sampling associated with the standard wavelet based multi-resolution algorithms reduces the capability for feature detection and analysis. To overcome

sub-sampling of an under sampled image, multi-resolution analysis can be accomplished through an over-complete "frame" representation and is carried out across an over sampled multi-resolution frame representation. An algorithm that uses frame representations of an image obtained with an autocorrelation shell of wavelets(AsW) was implemented. A new image extrapolation algorithm that uses the growth or decay of transform coefficients to generate sub-pixel information has been implemented. The magnification procedure results in an image with very low artifacts and outstanding presentation of contrast detail. This dissertation demonstrates the effectiveness of the AsW algorithm in extrapolating under sampled LWIR and medical x-ray images.

CHAPTER 1
INTRODUCTION

A Compton backscatter imaging (CBI) system operates somewhat like an optical visual system, where the reflected photons from the surface of the objects are converted into an electrical signal and processed to form an image. The CBI technique using x rays has been applied successfully to commercial products such as airport luggage scanning systems,[1] COMSCAN[2] tomography systems and developmental systems for the functional imaging of the heart.[3] There are other CBI applications such as COMTEL(Compton telescope),[4] void fraction measurement in two-phase fluids[5] and non-invasive evaluation of coronary bypass grafts that use the spectral analysis of the scattered photons to image objects.[6]

All the above mentioned CBI systems rely on first-scattered photons from the object to form images. The majority of the listed CBI applications also use only the first-scatter photons to generate images of the regions underneath the object surface. The surface imperfections and ridges affect the CBI image quality because these features can prevent first collided photons from reaching the detectors and lead to multiple-collision photons which now enter the detectors. Because of this obstruction and corruption, the CBI images of an object with unknown surface imperfection do not uniquely represent the surface and the regions underneath. Hence, slow running complex algorithms are necessary to extract useful information. Additionally, the dependence of CBI systems on first-collision backscatter photons to form images also imposes a constraint on detector size, detector collimation, and mode of detector operation. This limitation often leads to high source strength and slow imaging system operation.

A unique variation of CSI called Lateral Migration Backscatter Radiography (LMBR)[7,8,9,10] was developed at the University of Florida. One such system has been applied to detect plastic landmines buried in soil. As the name suggests, this modality uses the lateral transport of multiple-scattered photons in materials to form images. This modality uses large area detectors in current mode which helps in reducing the required x-ray source strength and image acquisition time. LMBR systems typically use two sets of detectors to form images. The first set of uncollimated detectors image predominantly first-collision photons and a second set is collimated and placed so as to image predominantly multiple-collision photons. The uncollimated detectors primarily generate images of the surface features. The contrast in the collimated detector images is due to multiple scattered photon lateral transport. This lateral transport is sensitive to the electron density of the transport medium as well as the surface spatial details. This phenomenon enables us to image objects that contain clusters of subtle imperfections and discontinuities in electron density and identify such electron density differences through contrast in collimated detector image. The multiple-collision photons always carry the information from the first-collision. However, with the increase in the number of collisions, multiple-collision components average out small sized electron density variations while retaining the information from the large sized discontinuities. Because the LMBR images are no longer restricted to first-scatter photons, this modality is useful for imaging objects even in the presence of surface clutter.

This research studies the details of photon transport in a LMBR system using the Monte Carlo technique and explains both qualitatively and quantitatively the reasons for the image contrast and features due to lateral photon migration. On the basis of the photon transport study, a unique LMBR image restoration algorithm and a Monte Carlo based lateral transport simulation algorithm (PLMS) are developed. An x-ray generator simulation program, XSPEC, is developed to facilitate the generation of x-ray spectra for LMBR systems study. Additionally, results from the LMBR photon transport study are used to arrive at optimum x-ray source and detector specifications for a representative LMBR system. This research not only lays the foundation for the development of other applications using LMBR but also demonstrates the methodology for optimizing the performance of an LMBR system.

Typical LMBR images have low-resolution, and extracting features from low-resolution images accurately is difficult. To facilitate the feature extraction from such low-resolution images overcomplete frame representations of an autocorrelation shell of wavelets (AoW) transform coefficients of a low-resolution image is used. This representation lead to the development of a new algorithm for image extrapolation based on the growth or decay of transform coefficients. This algorithm expands a given image to the next resolution scale without blurring the edges and presents an image with outstanding contrast details. Additionally, this representation also helps in multi-resolution feature enhancement. The AoW algorithm is applied to both LMBR images and images from other modalities to demonstrate its capabilities. The image expansion and feature enhancement algorithms have a wide area of application ranging from remote sensing to digital video image enlargement.

The various applications of CBI along with their features are discussed in Chapter 2. Chapter 3 presents the theory behind the Monte Carlo technique for studying photon transport and discusses the general purpose Monte Carlo computer code MCNP. Chapter 4 presents the theory of lateral migration in LMBR systems. Chapter 5 discusses the x-ray spectra generation computer program and its validation with measurements. Chapter 6 presents algorithms developed for the LMBR image restoration and the LMSR simulation algorithm PLMS. Chapter 7 discusses the algorithms developed for multi-resolution feature enhancement and transform based sub-pixel estimation and demonstrates the successful application to LMSR landmine detection. Chapter 8 summarizes the results of this research and lists the recommendations for future work

CHAPTER 2
OVERVIEW OF SCATTER RADIOGRAPHY

Three processes are responsible for the photon interaction with matter. They are photoelectric absorption, Compton scattering and pair production. Additionally, there are some minor effects such as Raleigh scattering, Thomson scattering by the nucleus, Delbruck scattering and nuclear resonance scattering and photodisintegration of nuclei. Quantum mechanics makes it possible to derive formulae for the probability of each process per unit tracklength and this probability can be expressed as a coefficient or as a cross section. The total cross section is the sum of the cross sections for the three different processes

$$(2.1) \qquad \sigma_t(E) = \sigma_{photoelectric}(E) + \sigma_{compton}(E) + \sigma_{pair\,production}(E)$$

These cross sections are dependent on the photon energy and the electron density in the material.

In the photoelectric process, all the incident photon energy is transferred to the bound electron which is ejected from the atom. This interaction probability increases with atomic number (Z) of the material and varies approximately as Z^3. This interaction is prominent at low energies. At very high energies($E>1.02$ MeV), the incident photons interact through pair production and are absorbed by the atoms to release positrons and electrons. This interaction has increasing probability at energies above its threshold at 1.02 MeV and varies as Z^2.

As the name suggests CSI relies on Compton scatter to generate images. In simple terms Compton scatter can be understood as a relativistic billiard ball collision between incident photons and the electrons after which the photon energy and angle change. The energy of the scattered photon is given by

$$\alpha' = \frac{\alpha}{1 + \alpha(1 - \mu)} \tag{2.2}$$

where α and α' are the incident and scattered photon energies, respectively, expressed in terms of electron rest mass and μ is the cosine of the scattering angle. The Klien-Nishina differential scattering cross section (equation 2.3) gives the probability of scatter from free electrons in a given direction.

$$\sigma(\alpha, \mu)d\mu = \pi r_0^2\left(\frac{\alpha'}{\alpha}\right)\left(\frac{\alpha'}{\alpha} + \frac{\alpha}{\alpha'} + \mu^2 - 1\right)d\mu \quad (\mathrm{cm}^2/\mathrm{electron}) \tag{2.3}$$

The above two equations form the basis for defining Compton scatter from a material. The scattering probability from a material is quantified by

$$P_s = \frac{\sigma_s}{\sigma_t} \tag{2.4}$$

where σ_s is the scattering cross section and σ_t is the total cross section of the material. The total cross section is the sum of the absorption cross section, σ_a, and the scattering cross section. σ_a is the sum of the photoelectric cross section which is high at very low energies and the pair production cross section which increases with the photon energy. From the discussion following equation 2.1, it can be said that both the photoelectric and pair production cross sections increase as Z^n, where n is greater than 1. However, the scattering cross section σ_s increases only as Z and it decreases with photon energy. Thus, from equation 2.4 it can be said that P_s is higher for low Z materials than for high Z materials.

As an example, P_s for a typical soil (Z=11) and a typical plastic landmine mine (TNT) (Z=7) are compared in Figure 2-1. It is clear from this figure that for the energy range of 20 -200 keV, the P_s value for mine (a low Z material) is more than that for soil; beyond this energy range the P_s values for these two materials are very close. This is because beyond this energy range, the absorption cross sections for soil and mine are very close to each other and have a larger effect than the scattering cross section. However, when steel (Z=26) is compared with soil and plastic it is clear that the P_s for steel is lower than that of soil and mine for the energy range between 20 -300 keV.

Using this sensitivity of photon scatter to Z, many imaging applications of Compton scatter have been developed. These applications are generally referred to as scatter radiography in the literature. This chapter reviews these applications and their utility under specific situations.

COMSCAN

The COMSCAN[2] application uses Compton backscatter to generate images. A schematic of this radiography system is presented in the Figure 2-2 a.[2] This system uses x-rays for the photon source and a set of scintillation detectors that view the backscattered photons through an aperture to image objects. Using the detector signals, depth information for an object is generated. To facilitate good statistics in signals, both aperture and detectors are kept near the surface. Figure 2-2(a) shows that COMSCAN uses single-scatter photons to generate images. This essentially limits the depth-of-view in the material to a photon mean free path. This modality can be applied only to image smooth surfaces because multiple-collisions from the surface would destroy the one-to-one correspondence between detector signal and depth. This system is now commercially used for nondestructive examination of airplane components.

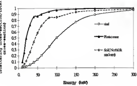

Figure 2-1 Comparison of scattering probabilities of three materials.

Coherent X-ray Scatter Tomography

At very low photon energies, photon scattering interaction is called coherent scattering. The electrons in an atom are considered bound for describing this interaction. This interaction cross section is given by[3]

$$\frac{d\sigma}{d\Omega} = \frac{d\sigma}{d\Omega}(\text{Thomson}) M_0 S(x) F^2(x, Z) \tag{2.5}$$

$$\frac{d\sigma}{d\Omega}(\text{Thomson}) = \frac{r_e^2}{2}(1 + \cos^2\theta),$$

where r_e is the classical electron radius and θ is the scattering angle. The Thomson differential cross section is modified by F, the atomic form factor, M_0 the atomic density, and S, the structure interference function. Here $x = \sin(\theta/2)/\lambda$, where λ is the wavelength of photons and θ is the scattering angle.

The atomic form factor F is related to the spatial distribution of electrical charge by a Fourier transform. The form factor gives a good description of coherent scattering when the phase relationship between atoms is not constant and interference effects are averaged over time. In the case of solids, we have to consider the interference due to coherent scattering from neighboring atoms. This effect is given by S(x) and shows sharp peaks when the Bragg scattering condition is satisfied.[3] These peaks can be used to identify the structure of the material causing the interference. In contrast, a material like liquid water does not show any sharp peak in its coherent scattered spectrum.

From the above equation we can see that the scattering probability is dependent on the molecular structure of the material. Using this principle, applications have been developed to image amorphous materials. The schematic of a system using coherent x-ray scatter

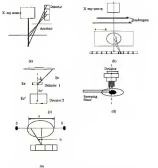

Figure 2.2 Scatter imaging applications, (a)CONSCAN (b)X-ray scatter tomography (c)COMTEL (d) Dynamic radiography (e)Compton profile

tomography is presented in Figure 2-2(b). The spikes in the x-ray diffraction spectrum are used to distinguish plastic explosives from ordinary plastic. This modality is used at airports to image explosives in luggage. However, this modality will not function for crystalline material because the peaks will be so close that these peaks cannot be resolved as separate peaks. This modality also relies on single-scatter photon interaction to achieve x-ray diffraction.

COMTEL

COMTEL[8] is an acronym for Compton telescope. It can be seen from the schematic in Figure 2-2(c) that this system uses two sets of detectors. These detectors operate in coincident mode. Using the Compton scatter equation 2.2 and the energy balance

$E_r = E_e' + E_e''$,

where E_r is the incident radiation energy,

E_e' is the energy deposited in the first detector and E_e'' is the energy deposited in the second detector.

The energy incident on the second detector is given by $Er' = Er - Ee'$.

A cone with an angle ϕ is constructed around the origin of the gamma source for each detector. Using similar pairs of detectors and maximum likelihood estimate, the origin of the gamma source is reconstructed. Because these detectors have a wide field-of-view, images of gamma sources in distant planets or stars can be reconstructed. This telescope is presently in operation at the Compton observatory. This principle is also used in gamma cameras to image and characterize nuclear waste. The angle ϕ and E_r are calculated based on the assumption that the gamma rays undergo single scatter in the front detectors. If there are multiple-collisions in the front detector, then the image of a gamma source has to be corrected for multiple-scatters.

Dynamic Radiography

The dynamic radiography system[7] is shown schematically in Figure 2-2(d) This system is now under development for functional imaging of the heart and it uses Compton scattered photons at 90 degrees to generate an image A voxel is formed by the intersection of detector field-of-view and the sweeping x-ray beam. The sweeping beam generates images of a moving surface and by moving detectors, the location of the surface-of-interest is identified. With the detector at this position the scattered photons are detected and the image of a moving surface is constructed Again, in this application the detectors are collimated to view only the first-scatter photons. The multiple-collision photons make dynamic radiographs noisy and speckled. A variation of this method that uses emission gamma rays and spectral analysis to image functions of coronary grafts is also under development

Compton Profilometry

An application of a Compton profilometry system[8] is presented in Figure 2-2(e). This system uses high resolution, high purity germanium detectors. The spectra from two gamma source positions S and S' are gathered.

The detected photon spectra D(E) from this system is given by

(2.6) $D(E) = \varepsilon(E)\ A\ \phi^1(r,E)\ \sin\theta\ B(E)$

where $\varepsilon(E)$ is the detector efficiency, A is the detector area, θ is the scattering angle, B (E) is the correction for multiple-scattered photons and $\phi^1(r,E)$ is the single scatter photon flux.

The density of the fluid $\rho(r)$ along the chord length z is obtained using the equation

(2-7) $$\ln\left[\frac{f}{D(E)\Omega(E)}\rho(x)\right] = A_p + A_s$$

where f is the total number of primary scattered photons from the material along chord length x, A_p is the optical path length for primary scattered photons and A_s is the optical path length for the multiple-scattered photons.

Applying an iterative algorithm and multiple-scatter corrections for each detector signal, the density profile along chord SS' (see Figure 2-2e) is obtained. A contour map of density can be generated by rotating source and detectors around the imaged object. This system limits the size of an imaged object to about one mean free path and considers signals predominantly from first-scatters. The detector signals have to be corrected for multiple-collision photons by applying an elaborate scheme.

Lateral Migration Backscatter Radiography (LMBR)

A system that uses multiple-scatter photons to generate images was developed at the University of Florida.[7, 8, 9-10] This modality is appropriately called Lateral Migration Backscatter Radiography (LMBR). A schematic of an LMBR system is shown in Figure 2-3. This system uses a pair of uncollimated detectors and a pair of collimated detectors to generate four images of an object.

The earlier discussion following equation 2.4 has shown that P_s is higher in low z regions than in higher z regions. This higher P_s is due to a relatively higher σ_s compared to σ_a which makes the mean free path (m.f.p) of scattered photons larger in low z regions than in

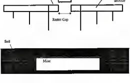

Figure 2-3 Schematic of the LMBR landmine imaging system.

higher Z regions. The m.f.p is larger for low density and low Z materials than the high density low Z materials. This difference in the photon travel path causes more multiple-scattered photons to reach the collimated detectors from lower electron density regions than from higher electron density regions. Because of this difference in number of detected multiple-scattered photons, the detector energy deposition is higher when the source is over a lower electron density region. The difference in detector energy deposition is observed as image contrast in LMBR images. This contrast in LMBR images can be used to identify these low electron density regions in a higher electron density medium. The utility of such a system to detect buried landmines in soil has been proven and the application of such a system for nondestructive testing of castings up to multi-mean free path depths has been proposed. The detail of the photon transport and the contrast generation in LMSR is brought out in chapter 4 of this dissertation.

It is clear from this review that all "conventional" Compton scatter radiography systems rely on the first-collision photons to generate images. These systems require high detector collimation and a strong x-ray or gamma ray source. Additionally, this reliance on single-scatter photons restricts their application to objects with sizes of about one photon mean free path and known surface.

This dissertations studies multiple collision photon transport and explains the operation of a LMSR system that uses the information from multiple-scattered photons to image discontinuities in a medium with non-uniform surface. Knowledge of the details of multiple-collision scatter photon transport could be also used to improve the design of conventional scatter radiography applications. Additionally, it is possible that the detectors in some of the conventional scatter radiography systems could be redesigned to utilize the information from multiple-scatter photons.

CHAPTER 3
MONTE CARLO METHOD FOR PHOTON TRANSPORT SIMULATION

This chapter briefly discusses the Monte Carlo method for solving the photon transport problem and verifies the Monte Carlo simulation results with measurements for the landmine detection problem. Photon transport in a medium can be described by the Boltzmann transport equation (BTE). Approximate solution to the BTE can be arrived at through various numerical techniques. The Monte Carlo (MC) method is one such numerical technique. The MC method provides integral quantities of phase space variables such as photon energy and scattering angle at specific locations through stochastic estimation. There are numerous books and articles published on the MC technique; one comprehensive book by Carter and Cashwell[21] is used as a reference for most of the work described in this chapter.

In the MC technique the individual photon history is simulated as a simplified Markov random process, i.e., the previous locations and incident angles are irrelevant for calculating interaction probabilities at any given position. However, simple physical modeling often fails to provide accurate results because physical simulations often require excessive computer time. Additionally, many scoring techniques cannot be derived from purely physical quantities. So special variance reduction techniques and scoring techniques are derived to provide an acceptable solution to the BTE. A discussion that proves that the MC technique provides a solution to the BTE is presented in Appendix-A of this dissertation.

Because photon transport itself is a stochastic process, the direct simulation of this process has to be stochastic in nature. One of the basic advantages of the MC technique which must be brought out here is that the MC calculation can be carried out by simulating the physics of each photon at every point in the history of the photon. This allows the simulation to be carried out in smaller phase space than is required for solving the same problem by modeling the whole system as a single unit. Because of this, the MC simulation requires the correct description of geometry of each region and most importantly correct source description to begin the problem. The material composition has to be defined to calculate the cross-sections and the angular transfer description functions for a photon. Based on the above principles the mechanics of simulating photon transport is designed.

Mechanics of MC Method for Photon Transport Simulation

The mechanics of MC photon transport simulation can best be described by a flow-chart in Figure 3-1. This flow chart describes the photon transport simulation process in a mine detection imaging system. There are various schemes that are used to calculate the photon energy, angular direction, position, and weight. These schemes are brought out in the flow charts presented in Figures 3-2 through 3-4, respectively. The algorithms represented in these flow charts are used in chapter 6 of this dissertation.

Figure 3-2 represents the MC sampling method for simulation of photon scattering in a continuous energy domain. The probability density function that describes the secondary energy and the scattering angles is given by the Klien-Nishina distribution. The first part of the calculation uses a rejection technique due to Kahn[12] to calculate the scattered energy of the photon, based on which a scattering angle is calculated. The azimuthal angle is sampled from a uniform distribution since the Compton scattering is azimuthally symmetric. On the basis of this angle, the direction cosines for a photon path are calculated and

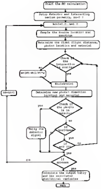
Start the MC calculation
Setup detector and interacting medium geometry, nn=0.0
kcol=0.0, w=1.0
Sample the source location and spectrum
Determine the first flight distance, photon location and material
Check if the interaction is scatter
no
w=(dt-da)/dt*w
yes
kcol=kcol+1
nn=nn+1
Determine new photon direction location and material
yes
Check if the photon is in detector
no
Tally the detector signal
if kcol<kmax
no
yes
if w<0.001
no
yes
no
if nn>nmax
yes
Calculate the output tally and its associated statistical variables
END

Figure 3-1 Flow chart for Monte Carlo simulation of photon transport

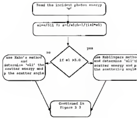
Read the incident photon energy 'e'
el=e/511 0; a=1/el;b=1/(1+2*el)
if el >3.0
no
yes
use Kahn's method and determine 'ell' the scatter energy and μ the scatter angle
use Koblingers method and determine 'ell' the scatter energy and μ the scattering angle
Continued in Figure 3 3

Figure 3-2 Monte Carlo scheme for calculating the scattering angle and energy of a photon

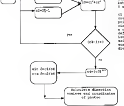

ξ the uniformly distributed random number between 0 and 1

c1 and c2 are coordinates of a point on the circumference of a circle defining the isotropic azimuthal scattering angle distribution

Figure 3-3 Monte Carlo scheme for calculating direction cosines and coordinates after each collision.

the new position is determined through the scheme as described by Figure 3-3; this process is repeated at each collision point.

Figure 3-4 provides a method for identifying the interacting material. It is clear from Figures 3-1 through 3-4 that this solution scheme is specific to a particular type of problem. However, there are many commercially available computer programs such as MCNP[11] (Monte Carlo n-particle) which handle general particle transport and provide various options for tallying the particle histories. The MCNP code has been used for simulating electron, photon and neutron transport problems. However, MCNP treats the collisional interaction of electrons and does not consider long range forces due to electric and magnetic fields. Additionally, such general purpose codes also provide flexibility in geometry description, source description and material definition. Because of this flexibility, the MCNP program has been chosen to simulate the particle transport in the LMBR system.

Because the focus of this research is to understand lateral migration backscatter imaging systems, the validity of MCNP results for the photon transport problems became relevant. The validation described below helped to provide confidence in the MCNP results and their relevance to the imaging system development.

Verification of the Suitability of the MCNP Random Number Generator for Solving Particle Transport Problems

The MCNP Monte Carlo radiation transport code uses a sequence of pseudo-random numbers to sample from probability distributions. The random numbers are selected from a known random number sequence and a set of random numbers in this sequence are skipped for each source

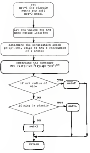

Figure 3-4 Monte Carlo scheme for determining the interacting material

particle. This set of random numbers skipped between each source particle is called 'stride' and is done to provide correlated sampling. In correlated sampling the two random walks are similar until one of the random walks is perturbed at which point the calculation causes the random sequences to diverge. Another random number selection technique that is used in MCNP is a tree-structured random number series. This scheme is useful for solving coupled particle problems. In this scheme, each type of particle starts with one random sequence, and if one of the particle's transport is deleted or modified, then the random walk for the other particle remains unaffected.

MCNP uses the congruential scheme of Lehmer to generate pseudo-random numbers.[14] In this scheme the starting integer of each history is

3.1
$$I_{n+1} = \mathrm{mod}(M^{*}I_{n}, 2^{48}) + 1$$
$$M = 5^{19}$$
$$S = 152917$$
$$R_{n} = 2^{-48}I_{n}$$

here S indicates the stride, R is the random number, and the period of this random number is about an half billion. This selection ensures that we have correlated sampling as well as random sequence for solving radiation transport problems.

The most important parameter to be verified is the quantity of random numbers used for simulating each particle history. The Table 3-1 compares the number of random numbers generated for typical electron transport and photon transport problem analyzed with MCNP in this dissertation. The electron transport simulation models the x-ray generation from a tungsten target and the photon transport problem simulates photon transport through a landmine imaging system. These problems are quite complicated and involve simulation of detailed energy, angle and position descriptions. It can be clearly seen from this table that the number of random numbers used for following each history is much less than the stride for the random number sequence; additionally, the total number of particles used is well below the period of this random number sequence. However, if a problem were to use more than 1/2 a billion histories then we have to input new M and S values into MCNP (equation 3.1) to alter this period. Thus, MCNP results should be acceptable as long as the cross-section data used are accurate and the material, geometry and the source distributions are correctly simulated.

Table 3-1 The number of pseudo-random numbers used for a typical MCNP simulation.

Type of problem	Number of random particles used in the problem	Number of random numbers used for the problem	Maximum number of random numbers used for any history
Electron/photon coupled transport problem	1 million particles	476,734,464	5842 for history 50183
Photon transport problem	2 million particles	1,059,226,419	7246 for history 348012

Validation of MCNP Results for a Sample Electron-Photon Transport Problem

To verify the MCNP results with measurements, the Maxitron x-ray generator was modeled. This problem is a coupled electron-photon transport problem and looks at the number of x-rays generated due to electron interaction with a tungsten target in a half-rectified x-ray generator. The results of this problem are strongly dependent on the simulation of the current and the voltage profiles for this generator along with various shielding materials associated with the photon travel path to the detector. The MCNP simulation is much simplified compared to the actual details of the Maxitron x-ray generator. The MCNP does not

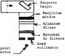

Figure 3-5a Setup of Maxitron x-ray generator used in MCNP electron-photon transport simulation

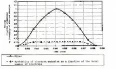

Figure 3-5b The voltage and the current wave form used in MCNP electron-photon transport simulation

consider e-e forces which play an important role in the operation of x-ray generators. The results from MCNP are compared with the measurements only to verify whether the order of magnitude of the MCNP prediction and the trends match with the measurements. The MCNP model of the x-ray generator is presented in Figure 3-5 along with the voltage and the current profiles used for this simulation. It is worth mentioning here that these voltage and current profiles are idealized for this x-ray generator for one active cycle and that there are jitters and other electrical disturbances associated with the x-ray generator which have not been considered in this simulation. A total of 1 million electrons and biasing for bremsstrahlung and characteristic x-ray generation are used in this simulation; the uncertainty of the MCNP results is about 6%. The point detector is at 30 cm from the tungsten target in the MCNP simulation and is scaled for the flux at 1 meter. The source strength of the x-ray machine is measured at 1 meter using a 2" NaI(Tl) scintillator detector collimated to avoid pulse pile-up. Figure 3-6 presents the experimental setup used for this test.

Table 3-2 compares the MCNP results with measurements for three settings of the Maxitron x ray generator. The calculations use a detector efficiency of 30% (detector efficiency is obtained from the detector manual). Considering the 150 and 175 kVp cases, measurements show a 135% increase in the source strength while MCNP shows only a 108% increase in the source strength. The Maxitron source is setup such that at high voltages (i.e., voltages ≥ 200 kVp) the current has to be 5 mA and above. This mode of operation lead to a high x-ray intensity from the Maxitron generator which caused the detectors to saturate. Thus the results at 200 kVp were unreliable. Table 3-2 shows that for a source kVp increase from 150 to 200, MCNP predicts 20% increase in source strength as against 148% from measurements. For 175 kVp to 200 kVp increase, MCNP shows 40% decrease in the source strength while measurements show a 5% increase in the source strength. The measured trends are not agreeable with MCNP results for 200 kVp source. The validation of MCNP with measurements will be again discussed in chapter 5, where the spectral characteristic of x-rays will be discussed.

The results in the Table 3-2 show that the MCNP predictions have

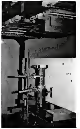

Figure 3-6 Experimental setup used for x-ray source strength measurement

an error ranging from about +50% to about -30%; however, the photon flux predicted is the same order of magnitude as the measured results.

The difference between the simulated and measured results may be because electron source of Maxitron x-ray generator is not a simple half-rectified source but an electron collector-discharger source, i.e., the cathode collects electrons during one half of the cycle and discharges during the next half of the cycle (at 1.2 kHz) to generate x-rays at the anode. Additionally, these collection-discharge processes are modulated by a 120 Hz current fluctuation. On the other hand, the MCNP model samples only a fraction of the total number of electrons (1mA=6.19E15 electrons/sec) actually interacting with the target using the probability distribution shown in the Figure 3-5b to give the number of x rays generated per incident electron. Using this predicted photon flux per electron, a linear relationship is applied to predict the photon flux at a given current value. Additionally, MCNP considers only the collisional electron interaction and does not consider long range e-e forces in the electron transport simulation. From the above analysis, it is clear that the MCNP simulation is an approximation that strongly depends on the radiation source description and treatment of electron interaction, but even under idealized source conditions it predicts the x-ray source strength of the same order of magnitude as in the actual system.

Table 3-2 Source strength comparison between MCNP and the Maxitron measurements.

case description	Measured value (particles/cm^2/sec/mA at 1 meter)	MCNP calculated value (particles/cm^2/sec/mA at 1 meter)	error(%)
150 kVp at 5mA	0.113E5	0.168E5	+48.7
175kVp at 10mA	0.265E5	0.336E5	+26.82
200kVp at 5mA	0.278E5	0.202E5	27.33

Validation of the MCNP Results Against Measurements for a Photon Transport Problem.

The system used for this validation is a x-ray backscatter landmine imaging system. The MCNP model and the experimental setup used for this validation are presented in Figures 3-7 and 3-8.

The landmine imaging system consists of a pair of uncollimated detectors placed near the source beam and another pair of detectors with lead collimators kept adjacent to these uncollimated detectors but farther from the x-ray beam.

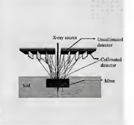

Figure 3-7 MCNP simulation of the photon transport in the landmine imaging system.

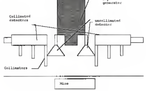

Figure 3-8 Measurement setup used for MCNP validation

To generate an image the x-ray beam rasters in the gap between the two uncollimated detectors and also moves with the detectors in a direction orthogonal to this raster direction. The two beam travel directions are called the raster and motion directions, respectively, and the gap between the two uncollimated detectors is called the raster gap. However, in the measured system the x-ray beam remains stationary and the sand-box moves in the above two orthogonal directions. This type of ground illumination is necessitated in the measurements because of the constraints related to the available x-ray generator.

The difference between the model and the measurement setup are:

1. The uncollimated detectors in the measurement are 2" closer to the soil surface than in the MCNP model.
2. The modeled uncollimated detectors are 140 cm long and 10 cm wide, whereas the detectors used for measurement are 30 cm long and 10 cm wide. The collimated detectors in the MCNP simulation are 140 cm long and 30 cm wide but 30 cm long and 30 cm wide in the measurement. The length is measured along the raster direction and the width is measured along the motion direction. The difference in the detector size between model and measurement is because of the difference in the x-ray beam motion between model and the measurement. It is important to note that the detector system motion modeled in the MCNP simulation is closer to that of the prototype LMBR landmine imaging system than the setup used for the measurements. This is because in both the MCNP simulation and the prototype LMBR system, the detectors move only in the motion direction with the vehicle, while the x-ray beam moves both in the vehicle motion direction and rasters orthogonal to this direction within the raster gap. This gives rise to edge effect or detector signal fall-off as the source is restored

towards the extreme end positions of the detectors. In contrast, in the measurement the sand-box motion is used to simulate the x-ray beam motion in both the vehicle motion and raster directions. In so doing, motion is also simulated for the detectors in both the motion and the raster directions. The source and the detector locations are thus always fixed relative to each other instead of experiencing a relative change in position in the raster direction. The measurements, therefore, do not exhibit edge effects or detector signal fall-off in the raster direction.

3. The detectors are modeled as NaI, and the energy deposition per source particle is used to generate the image. The model uses a smooth northfolk sea loam (NSL) soil with a TNT mine buried at 2.54 cm under the soil. The measurement system uses a soil similar to NSL but uses a TNT simulant for the explosive in the mine. The measurement system uses a pair of Bicron plastic scintillators for collimated detectors and Du-pont scintillation screens for the uncollimated detectors. Since we are displaying the results as pixel intensities in an image, this difference in the detector material will have minimal effect on the features observed in these detector images. The center of the landmine is at pixel location (16,16) and the image size is 33 by 33 for the measured images. MCNP simulates only half the size of the image which is symmetric about the 17th pixel position in the raster direction and the full image is generated by using the line of symmetry about this pixel position. This use of symmetry helps in reducing the time for the MCNP simulation to half.

The source strength for this validation is 175 kVp and 285,700 particles per pixel for both the collimated and uncollimated detectors. The uncertainties in the uncollimated and collimated detectors are 3.5% and 10%, respectively. The source spectrum used for this simulation is presented in Figure 3-8. The validity of this source spectrum for the

Maxitron x-ray generator will be discussed later in chapter 5. The result used for MCNP verification is an image of a 12" diameter plastic landmine buried at 1" depth-of-burial (DOB) in soil. The collimated detector images generated by MCNP and measurement are presented in Figures 3-10 and 3-11, respectively. The uncollimated detector images generated by MCNP and measurement are presented in Figure 3-12 and 3-13, respectively

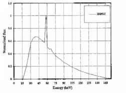

Figure 3-9 X-ray spectrum used for MCNP photon transport validation.

MCNP simulated Images

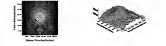

Front Detector Image

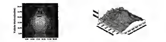

Rear Detector Image

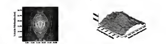

Sum of Two Detector Images

Figure 3-10 The MCNP generated collimated detector image of a 12" diameter plastic landmine buried at (17,17) and 1" DOB.

Measured Images

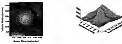

Front Detector Image

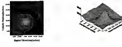

Rear Detector Image

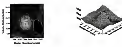

Sum of Two Detector Images

Figure 3-11. The measured collimated detector image of a 12" diameter plastic landmine buried at (16,16) and 1" BOS

MCNP simulated Images

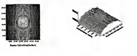

Front Detector Image

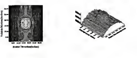

Rear Detector Image

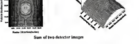

Sum of two detector images

Figure 3-12. The MCNP generated uncollimated detector image of a 12" diameter plastic landmine buried at (17,17) and 1" DOB

Measured Images

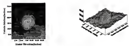

Front Detector Image

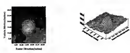

Rear Detector Image

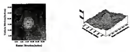

Sum of Two Detector Images

Figure 3-13 The measured uncollimated detector image of a 12" diameter plastic landmine buried at (16,16) and 1" DOB

The lines seen in the MCNP collimated and uncollimated detector images along the motion direction are due to the detector signal fall-off in the raster direction. This fall-off can be attributed to the reduction in the detector area seen by the scattered x-rays at the extreme pixel positions in the raster direction. The fall-off is about 60% in the collimated detector image and about 90% in the uncollimated detector images. It is obvious that this effect is more severe in the uncollimated detector images, and this is because these detectors have smaller widths (uncollimated detectors are 10 cm wide as compared to a width of 30 cm for the collimated detectors).

The front collimated detector images show lateral shift in the forward motion direction while rear detectors show an opposite shift. These shifts are 2" from the actual mine positions. The actual mine center was at 16" and 17" in the motion direction for the measurements and MCNP simulations, respectively. In the measured images the peaks are shifted to 19" and 13" in the motion direction for the front and the rear detectors, respectively. Similarly, the peaks are shifted to 19" and 15" in the MCNP images for the front and the rear detectors, respectively. The simulated uncollimated detector images do not show any significant shift either in the motion or the raster direction and the center of the mine is at (17,17) pixel positions in the simulation. The shift observed in the measured uncollimated detector images towards the rear in the motion direction is due to a slight slope that existed in the soil which cause the detector signals to be biased towards the higher side of the soil slope. Thus, the MCNP predicted images are comparable with those of the measurements.

To compare the MCNP and measured results for single line scans, the above setup without mine but with sloping soil was used. The MCNP results for soil slopes of 1" per foot and 0.5" per foot are compared here with measurements. Figures 3-14 and 3-15 compare the single scan line measured results with MCNP simulated results for 1/2" per foot slope for the motion and raster directions, respectively. MCNP simulates 4 million particles per pixel (in the motion direction) and the collimated detector signals have about 2% uncertainty and the uncollimated detector signals have <1% uncertainty. MCNP simulates NSL soil and the measurements used NSL+high Z sand to obtain the required slope. The MCNP simulations in the raster direction use a total of 295,000 particles per pixel. The uncertainties in the collimated and the uncollimated detectors are about 11% and 6%, respectively. The detector responses were generated through 2 MCNP simulations, each representing a half of the raster scan line. Figures 3-14 and 3-15 show that the trends of the MCNP results agree with the measured results. However, the MCNP uncollimated normalized detector response in Figure 3-14 shows a smaller drop than the measured results. This can be attributed to the fact that the soil used in measurements has higher Z than the soil used in the MCNP model, hence the MCNP signal is less sensitive to 1/2" per foot slope than the measured slope. The soil slope effects the signal intensity because of the decrease in signal intensity with an increase in the height of the uncollimated detector from the ground. If the detectors are kept farther from the ground, then the magnitude of the change in signal intensity is less for any small height variation than the change if the detectors were to be kept closer to the ground. The collimated detector signal shows a non-linear trend and it increases along the soil slope. This is because with an increase in the detector height from the soil surface, the collimators become less effective and hence allow more first and second-collision photons to interact with the detectors.

Figure 3-15 presents the detector response in the raster direction. The uncollimated detectors and collimated detectors show

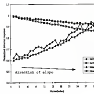

Figure 3-14 Single scan-line results of MCNP compared with measurements for 1/2" per foot slope in the motion direction

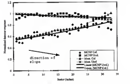

Figure 3-15 Single scan line results of MCNP compared with measurements for 1/2" per foot slope in the raster direction

similar response as presented in Figure 3-14. However, the detector signal fall-off can be seen in the uncollimated detector response. The trend lines are drawn through MCNP detector response data to compare these results with measurements. These trend lines agree well with measurements.

The simulation for 1" per foot soil slope case in the motion direction was done with 4.5 million particles per pixel and had an uncertainty of ± 5% for the collimated detectors and ±2 % for the uncollimated detectors. MCNP simulated results in the motion direction are compared with measured results in Figure 3-16. Both MCNP and measurements used the NSL soil for this comparison. It must be noted here that the direction of the soil slope is opposite to that of the soil-slopes in the rest of the single scan line plots. To show the data in a relevant scale, the responses were normalized to the highest of the two similar detector signals so that the information can be presented in the same plot. The change in the MCNP uncollimated detector signal due to the 1" per foot soil slope is within 3% of the measured change. The same parameter is within 18% of the measured value for the MCNP collimated detector result. The uncollimated detectors detect an order of magnitude more photons than the collimated detectors. This explains the probable reason for better agreement of the MCNP results with measurements for the uncollimated detectors.

Figure 3-17 compares the measured and simulated detector response for a 1" per foot slope in the raster direction. The MCNP simulation for this case was carried out using 200,000 particles per pixel for 17 pixels and the simulation was repeated for the next 16 pixels to generate 33 pixels. The uncertainties for the MCNP results are about 12% and 7% for the collimated and the uncollimated detectors, respectively.

The uncollimated detector signals have a fall-off similar to that observed for the 1/2" per foot slope (Figure 3-15).

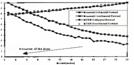

Figure 3-16 Single scan-line results of MCNP compared with measurements for 1" per foot slope in the motion direction

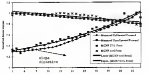

Figure 3-17 Single scan-line results of MCNP compared with measurements for 1" per foot slope in the raster direction

The trends in the MCNP results are similar to the measurements. The MCNP collimated detector scan-line signal agrees with the measurements and shows a non-linear increase along the direction of the slope.

MCNP single-scan line results with a 12" plastic mine buried under 1" of soil with 1/2" per foot slope are compared with the measured results in Figures 3-18 and 3-19 for the motion and the raster directions, respectively; the mine center is at 16". The shift in the position of the peak in the collimated detector response in the motion direction relative to the mine center is obvious in Figure 3-18, and the trends shown by the MCNP results match well with the measured results. The measured and the MCNP uncollimated detector responses do not show any shift in the position of the peaks in the detector response plots. Comparing these results from Figures 3-18 and 3-19, we can say that the signatures due to the presence of a mine are similar in both measurement and MCNP simulation results. The motion direction plots in Figure 3-18 show that the trends in both measured and MCNP detector responses agree and the position of the peak in the collimated detector response shows a shift of about 2" in the motion direction relative to the actual mine center. These simulations show that MCNP simulations produces similar results as in an actual imaging system and can be used to simulate the lateral migration backscatter imaging system.

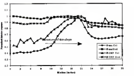

Figure 3-18 Comparison of MCNP single scan-line results with measurements for a 12 inch diameter plastic mine buried at 1" DOB with 1/2" per foot soil slope in motion direction

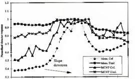

Figure 3-19 Comparison of MCNP single scan-line results with measurements for a 12 inch diameter plastic mine buried at 1" DOB with 1/2" per foot soil slope in raster direction.

CHAPTER 4
ANALYSIS OF PHOTON TRANSPORT IN A LMBR SYSTEM

In Chapter 3 it was shown that the Monte Carlo program MCNP[13] simulates photon interaction in a medium by random sampling from known probability distributions and simulates x-ray photon transport as in actual imaging systems. In this chapter the general purpose Monte Carlo computer code MCNP along with the photon track visualization code SABRINA[15] are used to study the photon transport in a LMBR system that images soil/landmine media.

SABRINA plots results from a MCNP Monte Carlo simulation with tracks representing particle transport paths. The tracks are filtered based on interacting cell, material, type of collision, and surface and can be color-coded according to the particle energy, time of production, and particle weight. These tracks can also be superimposed on the geometry of the transporting media so that the effect of each medium can be studied.

The collision tracks plotted by the original SABRINA represented cumulative collisions (i.e., a track plot of higher order collision was inclusive of all the lower order tracks). The original program was slightly modified to allow tracks to be traced based only on specified collision components. This modification facilitated the study of individual collision components.

To study the photon transport in a LMBR system the simulation of the landmine detection system is carried out for a case with the mine at a DOB of an inch and the source positioned over the mine center. The MCNP simulation uses 200,000 source particles and a 175 kVp spectrum.

out of which the first 30,000 particle events are logged. This results in a total of over 14,500 histories; the particle positions, collision number, energy, scattering angle, and weight for each event are logged in ASCII format in a PTRAC file. This file provides input for subsequent SABRINA simulations. It takes approximately 12 minutes on a SPARC-10 station to complete a track plot and a typical track file is approximately 38 MB.

The results from these analyses are then used to design detectors for the landmine imaging system that uses LMBR.

Analysis of Scatter Components in LMBR system

The results from the SABRINA simulation of the landmine imaging system are presented graphically as the plots of photon tracks. The number of tracks to be plotted was chosen such that they not crowd the track plot too much but represent the trends of quantitative results predicted by MCNP. Figure 4-1a and 4-1b represent the first-collision tracks from the mine+soil and mine, respectively. The plots represent 13671 histories/31203 tracks and 1230 histories/2739 tracks, respectively. These results are from the same simulation and show that only about 10% of the first scattered photons come from the mine. Figure 4-1a shows the effect of collimators in reducing the first-collision scatter energy deposition in the collimated detectors; the energy deposition in the collimated detectors is about an order of magnitude less than that of the uncollimated detectors. Figure 4-1a also shows that the majority of the first scatter photons originate from the surface and, hence, represent the surface features. The second-collision component tracks are presented in Figure 4-2a. This figure represents the scatters from the mine and shows 1158 histories/6340 tracks. There are essentially no second-scatter photons between 170-180°.

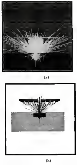

Figure 4-1 The first-collision components for a collimated detector a) all first-collision components b) first-collision components from mine

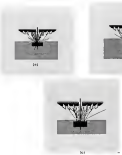

Figure 4-2 The collision components from mine a) second-collision b) third-collision c) fourth-collision

Additionally, most of the scatter photons are distributed very close to the incident beam and do not show any significant lateral transport in the mine.

The third and the fourth-collision component track plots are presented in Figures 4-2b and 4-2c, respectively. These plots represent 1155 histories/ 5957 tracks and 1159 histories/6699 tracks, respectively. Unlike first and second-scatter photons, these components show distinct lateral transport in the mine and these lateral transported components give rise to a secondary x-ray spot in the mine. The collimated detector images are dominated by the higher-collision components whereas the uncollimated detector images are dominated by the first-collision components. This imaging modality is referred to as *Lateral Migration Backscatter Radiography (LMBR)* because the image contrast in the collimated detectors is generated by a higher lateral migration of the multiple-scattered photons in a low Z medium.

Verification of MCNP-SABRINA Results with Analytical Calculations

To verify the observed angular distribution of scatter components and to calculate the scattering probabilities of Compton scattered photons the Klien-Nishina(K-N) cross-section relations are applied. On the basis of these K-N scattering probabilities, the average values of energy and scattering angles for scattered photons are calculated. The K-N scattering cross sections are first calculated for forward and backscattered photons. These calculated cross-sections are used to evaluate the average scattering angles and energies. The details of these calculations are presented as APPENDIX-B.

The results for the first Compton scatter are presented in Table 4-1 and Figures 4-3 and 4-4. In these figures and table, the average energy and scattering angle for forward and backscattered photons are given as a function of incident photon energy. It can be seen from Table 4-1 and Figure 4-3 that for the source energy between 40 -100 keV, the average energy of the forward and backscattered photons are nearly equal. The difference in the energies of forward and backscatter photons increases with an increase in the source energy. This energy range plays a very important role in LMBR because the average source energy for 120-200 kVp x-ray spectra is about 40-100 keV. The LMBR thus utilizes a source energy that yields an approximately equi-distribution of forward and backscatter energies for the first-scattered photons.

Table 4-1 The average scattering angles and energies of first scattered photons

F- Forward Scattered
B-Backscattred

Energy (KeV)	θ_F	θ_B	E_F	E_B
40	54.5	122.87	38.74	35.7
60	53.92	122.41	57.28	50.87
80	53.38	121.88	75.37	64.64
100	52.87	121.40	93.03	77.21
200	50.73	118.28	176.39	127.021
300	49.08	117.61	253.52	162.75
500	46.63	115.04	385.7	211.88
1.00E+03	42.57	111.21	711.66	288.46
5.00E+03	28.83	105.25	2832.12	383.448

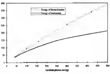

Figure 4-3 The average scattering energy for the first scatter photons

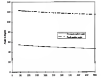

Figure 4-4 The average scattering angle for the first scatter photons

It can be seen from Figure 4-4 that for the energy range between 40-100 keV, average scattering angles for first scatter photons are nearly constant. Thus, for the monoenergetic source energy range between 40 - 100 KeV the average forward and backscattering angles can be approximated as 53° and 120°, respectively. The angular paths of first, second and third-collision backscattered photons (i.e., those photons that move toward the detectors) based upon average scattering angles are presented in Table 4-2 and Figure 4-5. The calculated results show a behavior that is similar to the SABRINA results. Thus, MCNP results represent the average behavior of x-ray photons in a scattering medium.

Table 4-2 Average scattering angles of the scattering components relative to the incident x-ray beam direction.
f=Forward
b=Backward

First collision	Second collision		Third-collision							
θ_b	θ_{fb}	θ_{bf}	θ_{fff}	θ_{ffb}	θ_{fbf}	θ_{fbb}	θ_{bbf}	θ_{bbb}	θ_{bfb}	θ_{bff}
122	175	174	162	-135	134	-110	132	-125	-120	-39

Detector Design for LMBR Landmine Detection System

The unique behavior of scattered photon collision components can be utilized to our advantage to design imaging detectors. The detectors used for LMBR are plastic scintillators/screen operating in current mode which enables us to measure the energy deposition in these detectors. These detectors are large area detectors and this helps not only in reducing the required source strength but also in averaging out the smaller background signal variations. The signal-to-noise ratio that defines the mine detectability in LMBR images is quantified by mine-to-*soil ratio (MSR)*.

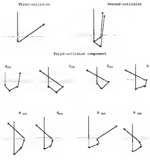

Figure 4-5 Schematic representation of collision component paths using average scattering angles.

The MSR is given by the relationship

$$MSR = \frac{E_{m+s}}{E_s} \quad \text{where,}$$

E_{m+s} is the energy deposited in a detector in the presence of a mine, E_s is the energy deposited in a detector in the absence of a mine (i.e., only from soil).

The principal design parameters that affect the performance of detectors are collimator lengths and raster gap size. The raster gap has a significant effect on the performance of the uncollimated detectors and since it dictates the separation distance between collimated detectors, it also effects their performance. Collimator lengths affect the performance of collimated detectors. Using the MSR and total energy deposition in the detectors, the design of the collimated and uncollimated detectors can be optimized.

Table 4-3 presents the effect of collimator length on energy deposition and MSR by collision components for collimated detectors with a fixed raster gap. These results are generated through a series of MCNP simulations of the landmine detection system. Table 4-3 shows that the MSR increases with an increase in the collimator length up to an optimum value and decreases beyond this value. The first-collision component and total energy deposition decrease with an increase in the collimator length.

Table 4-4 presents the effect of raster gap size on detector total energy deposition and MSR in the uncollimated detector from a series of MCNP simulations. The MSR increases slightly with an increase in the raster gap and the total energy deposition decreases by 47 % with an increase in the raster gap. As already stated, the increase in the raster gap also results in an increase in separation between collimated detectors and the source. This increase in separation distance in turn causes a decrease in energy deposition in the collimated detectors. The size of the raster gap is limited by the required total energy deposition in collimated detectors.

Table 4-3 Effect of length of the first collimator on the collimated detector performance.

Collimator length (cm)	Energy deposition by collision component					MSR
	1	2	3	4	All	
11	2.66e-9* (40.2)	1.66e-09 (25.1)	9.65e-10 (14.6)	5.57e-10 (8.4)	6.60e-9	1.45
12	1.24e-09 (31.8)	9.84e-10 (25.3)	6.73e-10 (17.3)	5.77e-10 (14.8)	3.89e-9	1.68
13.4	2.06e-10 (12.0)	4.22e-10 (24.7)	3.74e-10 (21.9)	4.17e-10 (24.4)	1.70e-9	2.09
14	1.28e-10 (9.2)	3.14e-10 (22.5)	3.28e-10 (23.9)	3.79e-10 (26.9)	1.39e-9	2.03

*Energy deposition is in MeV/gm per source x-ray
(values in parentheses are fractional energy deposition)
Detector width is 25.4 cm and mine DOB =2.54 cm;
400,000 source particles and ~ 4.8 % uncertainty in detector total energy deposition values.

Table 4-4 Effect of raster gap size on the uncollimated detector performance.

Raster Gap (cm)	Energy deposition by collision component					MSR
	1	2	3	4	all	
10	2.94e-08* (55.26)	1.15e-08 (21.62)	6.04e-09 (11.35)	2.97e-09 (5.58)	5.32e-8	0.9
20	2.51e-08 (54.26)	1.02e-08 (22.17)	5.43e-09 (11.80)	2.52e-09 (5.48)	4.6e-8	0.9
30	2.10e-08 (53.57)	8.79e-09 (22.42)	4.67e-09 (11.91)	2.29e-09 (5.84)	3.92e-8	0.92
40	1.65e-08 (52.38)	7.15e-09 (22.69)	3.96e-09 (15.84)	1.90e-09 (6.03)	3.15e-8	0.94

*Energy deposition is in MeV/gm per source x-ray
(values in parentheses are fractional energy deposition).
Detector width is 25.4 cm and mine DOB = 2.54 cm;
300,000 source particles and ~ 1.69 uncertainty in detector total energy deposition values

To visualize the effect of collimator length and raster gap size on the collision components, the photon transport in a landmine imaging system without collimators was simulated using MCNP/SABRINA. The results are presented in Figures 4-6. Figure 4-6a represents the 8600 first-collision tracks from 3850 histories. The second and third-collision plots are presented in Figures 4-6b and 4-6c, respectively. These figures represent 3877 histories/ 7940 tracks and 3886 histories/ 7500 tracks, respectively. The collimator shown in these plots was superimposed artificially on the track plots. It can be seen from these plots that the collimator with length shorter than the critical length is ineffective in stopping the surface scattered photons; however, a collimator with length greater than the critical length eliminates not only the scatters from the soil but also the scatters from the mine. Additionally, collimators with larger than critical lengths reduce not only the first scatter photons but also a significant amount of higher-collision photons. The above observation agrees well with the earlier observation that the MSR first increases with increasing collimator length and then decreases with an increase in the collimator length beyond the critical value. It can be seen from the Figures 4-1a and 4-6a that scatters from the surface do not show much lateral transport and, hence the first collimator is more effective in reducing the signals from surface features in collimated detectors. From the MCNP simulations, the first collimator is found to be responsible for removing approximately 55% of the photons that would otherwise reach the detectors; the second and third collimators combined remove approximately an additional 35% of the photons that would otherwise reach the detector.

As we have seen earlier from Table 4-4 and the Figures 4-1a and 4-6a, the number of first scatter photon tracks decreases with an increase in the raster gap size. An optimum raster gap is obtained by

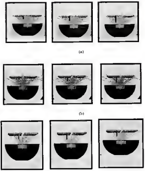

Figure 4-6 Effect of collimator length on the collision components (a) first-collision component (b) second-collision component (c) third-collision component.

increasing the raster gap size so as to reduce the first-collision component and thereby increase the MSR while maintaining an acceptable signal strength in the collimated detectors. Table 4-5 presents the detector design parameters for an optimized detector setup that is symmetric with respect to the source location and at a height of 30 cm above the ground.

Table 4-5 The design parameters for an optimized detector with a symmetric source position and detector height of 30 cm above the ground.

Parameter	Uncollimated detector (cm)	Collimated detector (cm)
Raster Gap	7.00	14.60**
Detector size* (L X W)	10.16 X 30	30 X 30
Collimator lengths	None	13.39,9.5,7.4***

* This detector size is specific to the available experimental setup.
** This dimension is the collimated detector separation.
*** The collimators are separated from each other by 10 cm.

Features in LMBR Images

Figures 4-7 and 4-8 present the MCNP images of a plastic mine, metallic mine and a pot hole for both front collimated and front uncollimated detectors, respectively. These images are used as examples to describe how these image signatures can be used to discriminate mines from other objects.

Consider Figures 4-7a and 4-8a which are the images of 30 cm diameter plastic landmine. The spread of the x-ray spot in the mine due to transverse travel of photons in the plastic mine results in a shift in the peak observed of about 3 inches the forward direction in the front collimated detector panel. Figure 4-9 presents schematically the physics that explains the shift based on the size of the spot. It can be seen from Figures 4-2b and 4-2c that the spread in the spot is approximately $2/3^{rd}$ the size of the six inch radius mine or approximately four inches in radius. When the source position moves to the edge of the mine, part of the spot is now in the soil and the photons originating from the spot now interact more with the soil. The soil being a greater absorber than the mine reduces the number of photons reaching the detector over the soil, thus leading to the asymmetry in the signals between the two detectors.

We can idealize the spot in the mine due to higher-collisions as a 2π disc source with a diameter that increases with the number of collisions. When the spot is closer to the edge of the mine, it is no longer a symmetric 2π disc source and is now an asymmetric source with a higher strength in the region that is in the higher scattering medium (mine). This causes the asymmetric variation in signal intensity. This shift is not seen in the raster direction because the detector is not collimated or segmented into two panels in the raster direction. This shift is much more prominent in the collimated detectors because these detectors see mostly the photons originating from the higher-collisions, i.e., from the larger spot in the mine than the uncollimated detectors. The image shifts in the front and the rear collimated detectors that are discussed above can also be seen in the measured images presented in Chapter 3 as Figures 3-10 and 3-11. A similar but opposite shift occurs in the rear collimated detectors. Thus it can be said that the shift observed in the collimated detector images is due to the lateral migration of scattered x-ray photons.

In the case of metallic mines (Figures 4-7b and 4-8b), the top metallic cover attenuates most of the lower energy signals; the energy

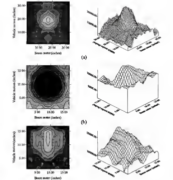

Figure 4-7 MCNP generated images from front collimated detector a)12 inch diameter all plastic mine located at (17,17) and 1 inch DOB (b) 12 inch diameter plastic mine with metal casing at (9,9) and 1 inch DOB, (c) a 12 inch diameter pot-hole 1 inch deep at (9,9).

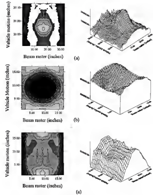

Figure 4-6 MCNP generated images from front uncollimated detector a)12 inch diameter all plastic mine located at (17,17) and 1 inch DOB (b) 12 inch diameter plastic mine with metal casing at (9,9) and 1 inch DOB, (c) a 12 inch diameter pot-hole 1 inch deep at (9,9)

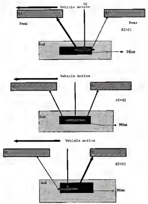

Figure 4-9 Schematic representation to demonstrate the reason for the peak shift in LMBR images.

deposition in the collimated detectors is due to higher energy components. These higher energy components originate from lower order collision components that have a smaller spot size. This makes the signal more symmetric and makes the metallic lining edge effect less significant. This explains why we do not see a significant shift in the image in the case of small metallic lined mines. Additionally, the scatter from the metal encased mine is lower than that from surrounding soil. This leads to a lower signal at these pixel locations both in collimated and uncollimated detector images.

In the case of a pot-hole, the mean free path for scattered photons is higher than the mean free path in plastic. This leads to larger transverse travel of multiple-collision components than in a mine. This makes the edge effects for a pothole more significant and explains the larger shift in the peaks in the case of pot-holes. However, a decrease in image intensity is noticed in the uncollimated detector images. This decrease in signal intensity over a pot-hole is due to an increase in the solid angle of detectors with respect to the scattering surface.

Consider now the case of a surface-laid object. The signal that the collimated detector sees is now mostly due to lower order collision components, i.e., to first and some second-collision components. These collision components have little transverse travel distance in the object. This means that we have less edge effect. This explains why no shift is observed in the images of surface-laid objects.

The measured front collimated and uncollimated detector images of a 6 inch diameter mine with metal casing are presented in Figures 4-10(a) and 4-11(a), respectively. These images show the same features as the MCNP generated images, i.e., the metal mine shows up as a decrease in pixel intensity in both collimated and uncollimated detectors. The measured images of a 12" pot-hole is presented in Figures 4-10b and 4-11b for collimated and uncollimated detectors, respectively. The measured pot-hole images show same features as MCNP images except that the measured pot-hole image is much smoother than the simulated image. The reason for this difference in smoothness between measurement and the MCNP simulation can be attributed to the straight pot-hole edges in the simulation compared to a smooth pot-hole edges in the measurements. Additionally, the MCNP detector signals are also affected by the detector signal fall-off.

By using the combination of collimated and uncollimated detector images along with image processing algorithms which will be discussed in Chapter 7, we can detect and differentiate plastic and metallic objects from voids and surface features.

It is thus summarized that the images of the buried landmines formed by the collimated detector are mostly due to higher collision components. The collimators designed on the basis of MCNP/SABRINA visualization are effective in reducing the first scattered photons. The first collimator is very critical in reducing the first-collision photons reaching the collimated detector.

The multiple-collision component detector signals of backscattered photons originate from spots due to transverse travel of photons in the scattering material. The size of the spot is proportional to the scattering cross section of the material. The higher the order of the scattering collision, the larger is the associated size of the spot. This secondary x-ray spot losses its symmetric property when it is close to the edges formed by two different scattering media. When higher order collisions make a significant contributions to the collimated detector response, this leads to asymmetric energy deposition in the two collimated detectors that is seen as a shift in collimated detector images of a buried object. The above discussion is summarized in Table 4-6 given below

Table 4-6 The summary of LMBR image features.

Material type	Collimated detector image	Uncollimated detector image
Low Z and low density (buried)	Peak in the detector image + shift in the peak	Dip in the detector image
Low Z and high density (buried)	Peak in the detector image + shift in the peak in opposite directions in two detectors	Peak in the detector image + no-shift in the peak
High Z and high density (buried)	Dip in the detector images	Dip in the detector image
Surface object	No-shift	No-shift

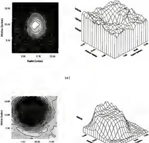

(a)

(b)

Figure 4-10 Measured images from front collimated detector (a) 6 inch diameter plastic mine with metal casing at (9,9) and 1 inch DOB, (b) a 12 inch diameter pot-hole 1 inch deep at (9,9)

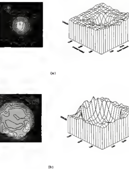

Figure 4-11 Measured images from front uncollimated detector (a) 6 inch diameter plastic mine with metal casing at (9,9) and 1 inch DOB, (b) a 12 inch diameter pot-hole 1 inch deep at (9,9)

CHAPTER 5
X-RAY SOURCE SPECTRA SIMULATION (XSPEC)

The x-ray spectrum is fundamental to any x-ray imaging system and it is necessary to predict x-ray spectra accurately for reliable modeling of an imaging system. The behavior of scattered photons dictates the contrast generated in LMBR images and, hence, the choice of x-ray spectrum is an important design parameter for a LMBR system. The x-ray spectra prediction program XRSPEC developed earlier by Campbell[16] was specific to the Maxitron x-ray generator. The XRSPEC program uses the following Kramer's relationship to generate the x-ray spectra,

5.1 $$E\,N(E).dE=Const.\,Z.(T-E).dE$$

where E is the x-ray photon energy,
N(E)dE is the number of photons generated for a finite energy interval dE, T is the electron kinetic energy and Z is the atomic number of the target.

Campbell corrected the bremsstrahlung spectra generated through Kramer's formula for photon attenuation in the target and used the product of integrated flux with a constant factor to calculate characteristic x-ray emissions. He incorporated various filters that modified the x-ray spectra. This computer program was later modified by Dodson[11] to simulate the pulsed MINX x-ray source.

Kramer's model, though very simple, often fails for small target angles. Several researchers have derived methods to simulate electron slowing down in x-ray generating targets along with the transport of the x-ray photons from such targets. Recently, Tucker et al.,[18] have derived a x-ray generation model specific to tungsten targets. Tucker et al., used semi-empirical relationships to model electron slowing down in a tungsten target and assumed a perpendicular incidence of the electron beam on the target. A detailed physics based model was recently published by Tan and Heaton [19] and their method models both an angular incidence of the electron beam and angular emission of photons from any target. The above two models were each validated with measured results for the energy range of 30-200 kVp. This energy range was selected for these models because of its importance in diagnostic imaging. Figures 5-1 and 5-2 present the sample data from Tucker et al., and Tan and Heaton, respectively. The characteristic x-rays that are expected to occur at around 60 keV for the tungsten targets are shown as discontinuities in these plots. As the applied voltage to a x-ray generator is increased the characteristic x-ray generation becomes dominant and needs to be modeled correctly. The characteristic x-ray spectra often determine the image quality because the x-rays in this energy range scatter better from low Z material. Because the x-ray generators used for IMBR are in the higher energy range of 150-250 kVp, characteristic x-rays play an important role and, hence, the models from Tucker et al.,[18] and Tan and Heaton[19] have to be slightly modified to include characteristic x-ray generation correctly.

A computer program, XSPEC, that uses some of the treatments from Tucker et al.,[18] and Tan and Heaton[19] has been developed. This model combines some of the semi-empirical relationships from Tucker et al.,[18] and the angular incidence of electron beam from Tan and Heaton.[19] A series of x-ray spectral measurements were made for the Maxitron x-ray generator using a EGT-high purity germanium detector and the results from XSPEC were compared with these measurements. Additionally, the Maxitron x-ray source was also modeled in MCNP with appropriate filters. This chapter describes the technique used for x-ray spectra measurements and the comparison of the XSPEC predictions with measurements and MCNP results.

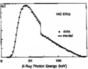

Figure 5-1 Comparison of experimental and computed bremsstrahlung spectra generated at 140 kVcp from Tucker et al.[38]

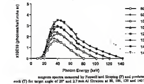

tungsten spectra measured by Fewell and Shuping (F) and predicted by current work (T) for target angle of 20° and 2.7 mm Al filtration at 80, 100, 120 and 140 kVp.

Figure 5-2 Comparison of tungsten spectra for a tungsten target at 20° angle and 2.7mm Al filtration from Tan and Heston.[18]

Computer Program XSPEC

As stated in the above paragraph, XSPEC assumes one-dimensional detailed electron slowing down in thick targets and considers the angular incidence of the electron beam and angular emission of x-rays from tungsten targets. The mathematical details of this computer program are briefly presented below.

The x-ray spectrum from a target can be written as

5.2 $I(E)dE = I_1(E)\ dE + I_2(E_k)\ dE$

Where I_1 represents the bremsstrahlung spectra and I_2 represents characteristic spectra and the E_k represents the K shell energy for characteristic spectra.

Calculation of Bremsstrahlung Spectra

The Bremsstrahlung spectrum is calculated through the following relationship

5-3 $$I_1(E) = \sigma_o \frac{Z^2}{A}\frac{dE}{E}\int_E^{T_0}\frac{B(T+m_0c^2)}{T}F(E,T)\left(\frac{1}{\rho}\frac{dT}{dx}\right)^{-1}dT$$

Here T is the kinetic energy of the electron,

E is the photon energy, T_0 is the kVp of the source and

σ_o= 0.58E-27 cm^2/nucleus

The Z and A stand for atomic number and atomic weight of the target, respectively

The $\left(\frac{1}{\rho}\frac{dT}{dx}\right)$ represents the stopping power of the target material

The factor B is a slowly varying function of Z and T is given by

5.4 $$B = (A + A_1 T_0)\left[1 + B_1\left(\frac{E}{T}\right) + B_2\left(\frac{E}{T}\right)^2 + B_3\left(\frac{E}{T}\right)^3 + B_4\left(\frac{E}{T}\right)^4\right] \quad E \leq T$$

and $B = 0$ $E > T$

where A, A1, B1, B2, B3, B4 are empirical constants and

T, the electron energy at any depth, is estimated through the Thomson-Whiddington relationship

5.5 $$\rho Cx = T_0^2 - T^2$$

where ρ is the density of the target material,

C is the Thomson-Whiddington constant ,

and x is the depth in the target.

The factor F uses the Thomson-Whiddington relation for electron penetration distance and it also includes the attenuation of the generated x-ray photons. It is given by

5.6 $$F(E,T) = \exp\left(\frac{-\mu(E)\,(T_0^2 - T^2)}{\rho C}\,\frac{Cos\theta_i}{Cos\theta_x}\right)$$

where μ(E) is the attenuation coefficient for the target material,

θ_i is the incident angle and θ_x the x-ray emission angle.

Characteristic Spectra Calculation

The characteristic x-ray generation increases with an increase in the difference between the electron energy and the k-shell binding energy. The k-shell binding energies and fractional yields considered in this model are presented in Table 5-1.

The characteristic x-ray generation is given by

5.7 $$I_K = Const \quad (T_0 - E_K)^{1.63}$$

Most of the characteristic x-rays are generated from the target surface, and as the electrons migrate deeper into a target, their energy decreases and hence the characteristic x-ray generation reduces.

Table 5-1 The fractional yield values used in XSPEC for calculating characteristic spectra.

K x-ray	Binding energy E_k(keV)	Fractional yield f
α_1	59.32	0.4500
α_2	57.98	0.2592
β_1	67.20	0.1521
β_2	67.1	0.0387

Equation 5.7 can be recast and modified to account for the cumulative probability distribution of characteristic x rays including the target attenuation to yield

$$5.8 \qquad I_2(E) = A_k\left(E_0 / E_k - 1\right)^{n_k} f(E)\int_0^R p\left(\frac{x}{R}\right)e^{-\mu(E)x\cos\theta_1/\cos\theta_2}dx$$

where A_k = (Const from equation 5.7)/$E_k^{n_k}$,

n_k=1.65

R is the distance at which the electron reaches E_k,

f is the fractional contribution of the characteristic x-rays,

'x' is the electron travel distance,

p is the probability distribution of the characteristic x-rays and

μ is the attenuation coefficient in the target

The angle θ_1 represents the electron incident angle and angle θ_2 represents the exit angle of the x-rays. The integrations in the above equations are implemented numerically in the computer program XSPEC. The program listing is presented in Appendix-C.

Measurement of Maxitron X-ray Spectra

To validate the results from the XSPEC spectrum prediction program, the spectra of the Maxitron x- ray generator are measured using a PGT-high purity germanium detector. To avoid damage to the detectors it was necessary to reduce the number of photons interacting with the detector below 100,000 counts/sec. A special lead collimator with a 0.0015 inch aperture and several aluminum filters were used to reduce the photon flux at the detector. The hi-purity Ge detector is located directly below the beam. The Table 5-2 presents the sizes of filters used in the spectrum measurements. Figure 5-3 presents the setup used for x-ray spectra measurements. The detection system was first calibrated using a 5mCi cobalt-57 source and a 300 mCi americium-241 source. These two gamma sources are selected because they have characteristic peaks at 120 keV and 60 keV, respectively (which are high-range and mid-range energies of the x-ray spectrum). Calibrating the counting system to this energy range assures accurate measurement of the x-ray spectra in the energy range that is important for the multiple-collision backscattering.

Table 5-2 Filters used for spectra measurements.

Filter position	Filter size (cm) 100 -150 kVp	Filter size (cm) 175-200 kVp
1	0.0217	0.034
2	0.6692	0.669
3	0.2769	0.988
4	0.055	0.055
5	1.76e-03	4.84e-03
6	---------	1.76e-03

The filter position 1 indicates the position closest to the source and position 6 is the position closest to the detector. The filters are also simulated in XSPEC and MCNP for predicting the x-ray spectra

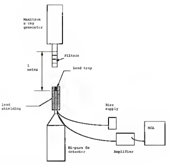

Figure 5-3 Schematic of the detection system used for x-ray spectra measurements

Monte Carlo Simulation of X-ray Source

The general purpose Monte Carlo code MCNP is used for simulating photon, electron, and neutron transport problems. The advantage of using this computer code is that detailed three dimensional simulations of complicated geometry can be done with ease. Hence, this code can be used to simulate the details of any x-ray source including the effect of filters and structures on the output spectrum. However, MCNP does not consider the long-range electric and magnetic forces for the electron-photon transport. Validated MCNP results would provide the confidence required to use MCNP for the design and analysis of the x-ray sources. The validation of MCNP results is conducted by simulating the Maxitron x-ray source, including the half- wave rectified voltage and current wave forms for the electron source as presented in Figures 3-5a and 3-5b.

The electron source in the Maxitron x-ray generator is not just a simple half-rectified source but an electron collector-discharger source, i.e., the cathode collects electrons during one half of the cycle and discharges during the next half of the cycle (at 1.2kHz) to generate x-rays at the anode. Additionally, these collection-discharge processes are modulated by a 120 Hz current fluctuation. On the other hand, the MCNP model supplies only a fraction of the total number of electrons (1mA=6.19E15 electrons/sec) actually interacting with the target using the probability distribution shown in the Figure 3-5b to give the number of x-rays generated per incident electron and does not consider the jitters and fluctuations associated with the actual power supply. A total of 1 million electrons are used in this simulation.

The filters presented in the Table 5-2 along with the lead collimator were simulated in the MCNP model. A point detector at 100 cm from the tungsten target is tallied in MCNP to calculate the spectrum

The point detector tally is a deterministic tally and it calculates the flux at a point based on the solid angle from a given x-ray emitting source position to the detector. This deterministic tally reduces the number of particles required for obtaining low uncertainty (<5%) tallies. It should be noted here that MCNP models an idealized detector, which has the same response for all photon energies, whereas the efficiencies for a real detector vary with photon energy and, hence, their sensitivity is not uniform through the spectrum.

Results and Discussion

The predicted XSPEC, MCNP and measured spectra were normalized for each Maxitron energy and shape indices results are compared in Table 5-3. To compare the shapes of the XSPEC and MCNP spectra with measurements, all spectra were normalized to the maximum spectral value. This normalization has to be carried out because MCNP tallies photon flux as photons per source history, XSPEC generates photon flux as photons per mA per steridian and measured units are in counts per channel.

To compare the predicted spectra with measurements a set of spectral shape factors were defined. They are

f1=Xb/Xc1,

f2=Xb/Xc2

where

Xb is the relative flux at bremsstrahlung peak Eb,

Xc2 is the relative flux at first characteristic peak Ec1,

Xc2 is the relative flux at second characteristic peak Ec2,

Table 5-3 Comparisons of shape indices for the Maxitron x-ray generator predicted and measured spectra

Energy (kVp)	Predicted Values XSPEC					Measured Values					Predicted Values MCNP				
	Xb/ Xc1	Xb/ Xc2	Eb	Ec1	Ec2	Xb/ Xc1	Xb/ Xc2	Eb	Ec1	Ec2	Xb/ Xc1	Xb/ Xc2	Eb	Ec1	Ec2
100	1.81	---	30	58	---	1.11	----	38	56	--	1.11	----	40	56	65
150	0.95	1.72	36	60	68	0.72	1.31	42	58	63	0.68	1.74	40	58	65
175	0.69	1.64	42	60	69	0.35	0.85	44	58	63	0.60	1.21	39	56	63
200	0.51	1.19	40	60	68	0.42	0.84	48	60	65	0.5	1.19	48	60	68

Note
Xb is the relative flux at bremsstrahlung peak
Xc1 is the relative flux at first characteristic peak
Xc2 is the relative flux at second characteristic peak
Eb is the energy at bremsstrahlung peak in keV
Ec1 is the energy at first characteristic peak in keV
Ec2 is the energy at the second characteristic peak in keV

Eb is the energy at bremsstrahlung peak in keV, Ec1 is the energy at first characteristic peak in keV, Ec2 is the energy at the second characteristic peak in keV.

From Table 5-3 it can be seen that XSPEC over-predicts the bremsstrahlung peak compared to the measured and MCNP bremsstrahlung peaks. The Xb/Xc1 value predicted by XSPEC differs by 63% with respect to measurement and MCNP for the 100kVp case. This value varies by about 32%, 77%, 21% with respect to measured results for the 150, 175 and 200 kVp spectra, respectively. The bremsstrahlung peak energy location predicted by XSPEC differs from the measured value by -21 % for the 100 kVp spectrum; however, this variation decreases with an increase in source kVp and agrees with the measured result for the 200 kVp spectrum. The XSPEC predicted energies for the characteristic peak are within about ±3.5% and ±9% of the measured first and second characteristic peak values, respectively. The XSPEC predicted Xb/Xc2 values differ by 31%, 52% and 41% with respect to the measured values for the 150, 175 and 200 keV spectra, respectively. The XSPEC predicted Xb/Xc1 and Xb/Xc2 values show a trend with the change in kVp of the spectrum that is similar to the trend exhibited by the MCNP and measured results.

It should be mentioned here that the lead collimator used in the measurement to cut down the number of interacting photons is not modeled in the XSPEC code. This lead collimator eliminates most of the low energy photons from the spectrum, considering the simplified model used in the XSPEC code we can say that the XSPEC predictions are closer to the measured results at higher energies.

The MCNP predicted Xb/Xc1 values differ by 0%, -3.6%, 54% and 19% with respect to the measured Xb/Xc1 values for the 100, 150, 175 and 200 kVp spectra, respectively. The MCNP predicted Xb/Xc2 values differ by 33%, 27% and 42% with respect to measured results for the 150kVp, 175kVp and 200 kVp spectra, respectively The agreement of MCNP results with measured results is better than for the XSPEC results because MCNP simulates the lead collimator in the detection system model. MCNP considers collisional interaction of electrons but neglects the electron interaction with the electric field and hence such disagreement between MCNP results and the measurements is expected when we use MCNP to simulate electron accelerators.

The XSPEC predicted Xb/Xc1 values differ from the MCNP results by 63%, 56%, 15% and 2% for the 100 kVp, 150 kVp, 175 kVp and 200 kVp spectra, respectively. The XSPEC predicted Xb/Xc2 values differ from the MCNP results by -1.2%, 16% and 8% for the 150 kVp, 175 kVp and 200 kVp spectra, respectively The XSPEC predicted bremsstrahlung peak energies differ from MCNP results by -33%, -11%, 7.6% and 0% for 100 kVp, 150 kVp, 175 kVp and 200 kVp spectra, respectively, The XSPEC predicted characteristic peak energies are within 10% of the MCNP results. As the source kVp is increased, the lead collimator used in the MCNP model becomes less effective which results in detection of most of the photons with energy above 30 keV. The good agreement between XSPEC and MCNP at higher energies indicates that the faster running XSPEC can be used for the x-ray spectra prediction at higher energies (>150 kVp) instead of MCNP.

The disagreement between MCNP and XSPEC results with respect to measurements is about 30–40% for most of the cases. This disagreement is due to the different approximations of the Maxitron electron model used in XSPEC and MCNP

The normalized XSPEC, MCNP and measured spectra are compared in Figures 5-4, 5-5, 5-6, and 5-7, for source energies 100 kVp, 150 kVp, 175 kVp and 200 kVp, respectively. It can be seen from these figures that MCNP results agree with measurements better than XSPEC results.

However, the trends predicted by XSPEC and MCNP follow the same trend as that of measurements. As a summary, it can be said that XSPEC predicted spectra have the same trend as measurements and MCNP. The MCNP allows detailed modeling of the filters and other devices in the photon path and hence predicts spectra closer to measured than the one-dimensional electron transport model such as used in XSPEC

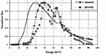

Figure 5-4 Comparison of XSPEC, MCNP and measured Maxitron x-ray spectra at 100 kVp.

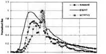

Figure 5-5 Comparison of XSPEC, MCNP and measured Maxitron x-ray spectra at 150 kVp.

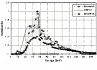

Figure 5-6 Comparison of XSPEC, MCNP and measured Maxitron x-ray spectra at 175 kVp

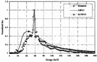

Figure 5-7 Comparison of XSPEC, MCNP and measured Maxitron x-ray spectra at 200 kVp

CHAPTER 5

APPROXIMATE SOLUTIONS TO THE LATERAL MIGRATION BACKSCATTER (LMB) PHOTON TRANSPORT

The MCNP Monte Carlo analysis in Chapter 4 has shown that the images formed in the collimated detectors are predominantly due to multiple-scattered photons and these photons originate from a secondary source in the scattering medium. Two approximate solutions to the lateral migration backscatter (LMB) photon transport from the x-ray source to the collimated detectors have been developed. The first method uses a deterministic approach and approximates the multiple-collision photon transport as a two-collision phenomenon. This model uses a pseudo-inverse solution to the photon transport problem to restore the LMBR images. The second method uses a specialized Monte Carlo solution to the photon transport problem. This Monte Carlo solution differs from MCNP because it uses some of the phenomena observed in Chapter 4 to approximate the Monte Carlo simulation and reduce the LMBR image computation time. This chapter discusses these two approximation methods and compares their results with measurements and/or with MCNP simulations.

Two-collision Model for LMB Photon Transport

A two-collision approximation was developed by Watanabe et al.,[6] to solve the LMB photon transport problem. This approximation assumes that a photon undergoes two 90 degree scatters before reaching the collimated detector. Watanabe et al., applied this model to predict mine parameters and restore LMBR landmine images.

The collimated detector response in a LMBR system is given by

$$F_c\left(x, y; x_0, y_0\right) = C_1\left[1 + \exp\left(-C_2\left(2h + e + \frac{H}{2}\right)\right)\left(\exp C_3 l(x, y; R, x_0, y_0)\right) - 1\right] + \eta \tag{6.1}$$

where

(x_0, y_0) = mine center,

(x, y) = pixel location,

h = DOB,

H = the mine height,

R = radius of the mine,

l = chord length through the mine of a line joining the x-ray source projection to the pixel projection (lateral photon transport length in a mine),

e = chord length through the soil of a line joining x-ray source projection to the pixel projection (lateral photon transport length in the soil),

η = additive noise $C_0\sigma$, where σ is the standard division of measured data with no mine,

C_1 = average measured detector response with no mine

C_2 = fitted parameter that represents the attenuation coefficient of the soil,

C_3 = fitted parameter that represents the difference in attenuation coefficient between mine and soil.

The above notations are also presented in Figure 6-1. The detector response F_1, is computed at four corners of a pixel of size Δx at

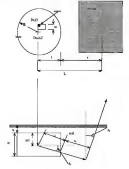

Figure 6-1 Schematics illustrating the notations used in the two-collision models.

location(x,y) and averaged to obtain the detector response D_1. The sum of the responses from two symmetric detectors are then calculated by

$$6.2 \quad D(x, y, h, R, x_0, y_0) = D_1(x, y, x_0, y_0) + D_1(x, 2y - y_0, x_0, y_0)$$

The error between the measured pixel intensity and the calculated detector response 'D' is minimized through the Lavenberg-Marquardt [26] fitting technique for estimating x_0, y_0, h and R values. These variables are referred to as mine parameters and Lavenberg-Marquardt technique minimizes the following equation

$$6.3 \quad \chi^2 = \sum_{i=1}^{I}\sum_{j=1}^{J}\left[\frac{D_m(x, y) - D(x_i, y_j, h, R, x_0, y_0)}{\sigma_{ij}}\right]^2$$

where D_m is the measured detector response at pixel (i,j),

D is the two-collision model calculated detector response, and

σ_{ij} is the measured standard deviation at pixel (i,j).

Watanabe's two-collision model was tested for various situations. Table 6-1 presents the results of one such test. It can be seen from Table 6-1 that the original two-collision model fails to predict both mine radius and location accurately (within 10% of the actual values) with a rock present on the surface.

Table 6-1 The mine parameter predictions of the original two-collision model.

Actual depth of burial	Surface feature	Predicted parameters			
		h	R	x_0	y_0
1	Smooth	1.02	5.45	8.47	8.63
1	rocks	1.35	4.82	8.8	13.2
2	rocks	1.52	7.37	8.28	10.13
3	rocks	2.58	8.84	5.71	9.38

All dimensions are in inches
The actual 6" radius mine was located at $x_0 = y_0 = 8$ inches

It was seen in Chapter 4 that the photons scatter in all directions and form a 2π disc source in the scattering medium. The

It was seen in Chapter 4 that the photons scatter in all directions and form a 2π disc source in the scattering medium. The photons that originate from this 2π photon source travel back to the detector to make energy deposition. The collision analysis in Chapter 4 using the average cross section has shown that the average energy of multi-collision backscattered photons is about 40 - 70 keV. We know that in this energy range the angular distribution of Compton scattered photons is isotropic. On the basis of this assumption, the scattering angles at the point of first scatter and second scatter can be calculated by random sampling from an uniform distribution. This led to a modification in the original two-collision model used for landmine image restoration. The modification involves 500 random samplings of cosines of scattering angles which are used to calculate the average scattering angles at the first and second scatter points. These values are then used to calculate the average chord length 'l_1' and the return distance 'h1' in the two-collision model (see Figure 6-1). The equation 6.1 can now be written as

6.4 $\overline{E}_1(x, y, x_s, y_s) = c_1[1 + \exp[-c_2(h + h1 + s_1)](\exp(C_3 l_1) - 1)] + \eta$

where

h1 $=(h+W/2)/\cos(\theta_2)$

l_1 $=l/\cos(\theta_1)$ and

s_1 $=s/\cos(\theta_1)$.

The other parameters used in this equation are presented in Figure 6-1. To test the performance of the modified two-collision model the cases used in Table 6-1 for testing the original two-collision model were used. Table 6-2 presents the results of this test.

Table 6-2 Predicted mine parameters with the modified two-collision model(all dimensions are in inches)

Actual depth of burial	Surface feature	Predicted parameters			
		h	R	x_0	y_0
1	Smooth	1.32	5.92	9.31	6.51
1	rocks	1.52	4.71	9.22	10.52
2	rocks	1.65	6.06	9.97	9.42
3	rocks	2.29	5.85	9.79	8.96

Comparing Tables 6-1 and 6-2 it is evident that the modified two-collision model predicts the mine radius and location better than the original two-collision model for all DOB's Thus, the modified two-collision model treats the photon lateral migration better than the original two-collision model. Moreover, the C2 and C3 values used in the modified model for this prediction are calculated using the actual soil and mine attenuation coefficients.

LMBR Image Restoration

The image restoration algorithm models the detector response

6.5 $D_i(x, y) = Q_i(x, y) + S_i(x, y)$

where i is the detector number,

Q is the signal due to the component traveling through the soil without passing through the mine,

S is the signal due to the component traveling through the mine and is approximated by the two-collision model presented in the equation 6.1 or 6.4.

It was shown in Figures 3-10 and 3-11 that the detector signal from a buried mine does not show any shift in the raster or X-direction, but it does exhibit a symmetric shift about the center line in the motion or Y-direction. Thus, we can write the approximation,

6.6 $S_2(x,y) \approx S_1(x, y-2y_0)$.

The signal from the soil is primarily due to first collision scatters at or near the soil and is symmetric with respect to the x-ray beam position in both the raster and motion directions and hence we approximate

6.7 $Q_2(x,y) \approx Q_1(x,y)$

Using the above approximations we can write

6.8 $(D_1 - D_2)^2 = \left[\varepsilon^2 + 2\varepsilon(S_1(x,y) - S_2(x,y))\right] - 4S_1(x,y)S_2(x,y) + \left[S_1(x,y) + S_2(x,y)\right]^2$

where $\varepsilon = Q_1(x,y) - Q_2(x,y)$

From equation 6.7 it can be said that ε is very small and hence equation 6.8 can now be written as

6.9 $(D_1 - D_2)^2 = \left[S_1(x,y) + S_2(x,y)\right]^2 - 4S_1(x,y)S_2(x,y)$

Recasting the above equation and using measured data for the D's, equation 6.6 can be written as

6.10 $\left[S_1(x,y) + S_2(x,y)\right]^2 = \left[D_1(x,y) - D_2(x,y)\right]^2 + \left[4S_1(x,y)S_2(x,y)\right]^{1/2}$

where the 'S' on the RHS is approximated by the two-collision model and 'S' on the LHS is the restored signal.

A measured, summed collimated detector LMBR image that has a wooden rod on the top of the mine and a rock at the edge of the mine was used to test the modified two-collision model for image restoration and is presented in Figure 6-2. The predicted values of the mine parameters from the original and the modified two-collision model are presented in

Table 6-3. The restored image using the improved two-collision model is presented in Figure 6-3 and the restored image using the original two-collision model is presented in Figure 6-4.

Table 6-3 Comparison of the mine parameter predictions by the modified two-collision model with the predictions by the original model for the test image.

Mine parameter	Actual values	Original two-collision model	Modified two-collision model
h	1	0.12(-88)	0.43(-77)
R_c	6	4.98(-17)	5.5(-8)
x_c	9	7.99(-11.2)	8.05(-10.6)
y_c	9	8.89(-1.22)	8.60(-4.4)

The values shown in parentheses are the errors in percent with respect to the actual parameters.
All dimensions are in inches.

The original model represents the mine as a circular object with jagged edges, whereas the improved model restores mine image as a symmetric circular object. The improved two-collision model works better than the original two-collision model for restoring the circular plastic object images.

Specialized Monte Carlo Model, Photon Lateral Migration Simulator(PLMS)

It has been shown in the Chapters 3 and 4 that photon transport in a LMBR system can be solved quite accurately through the general purpose Monte Carlo program MCNP. However, such general purpose programs carry lot of overhead in terms of computational requirements. For example, to generate a 33 X 33 LMBR image with MCNP simulation using ~ 500,000 particles per pixel requires approximately 32 hours of computational time on an IBM ES9000 mainframe computer.

The following are some of the reasons that slow down an MCNP simulation:

1. MCNP terminates a particle history according to particle weight and energy. However, MCNP cannot terminate a particle based on its collision, direction of travel or migration length. The MCNP allows user defined cell importance which is used to terminate a particle. By carefully adjusting the cell importance, one can selectively reduce the weights of the particles in those regions that are less relevant to the problem. This automatically forces the use of multiple cells in MCNP.
2. MCNP does not allow drastic changes in particle weight between two adjacent cells because it creates sudden jumps in the particle tallies. These sudden jumps reduce the precision in the tallied MCNP results. Hence many cells have to be defined with gradual reduction in cell importance.
3. To selectively tally collision based results in MCNP, one has to follow all the collisions and tally only those particles that have user defined collisions. This type of tallying is required because MCNP does not terminate a particle according to its collision number. Thus, for collision flagging tallies more particle histories have to be followed to obtain precise results. To avoid this, all collision particles are tallied in the detectors and the contrast generated due to multiple collisions are seen as LMBR images. The first two-collision components originate mostly from soil make the collimated

detector LMBR images noisy. So to obtain a good mine image one has to use many particle histories.

4. Additionally, the detailed physics modeling and cross-section data interpolation procedure are used in MCNP requires high input-output operation between the hard disk and CPU of a computer. These IO operations slow down the overall computational time.

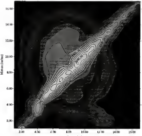

Figure 6-2 Image used for testing the modified two-collision model.

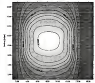

Figure 6-3 Restored image using modified two-collision model

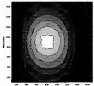

Figure 6-4 Restored image using the original two-collision model

To speed-up the computation of the direct Monte Carlo simulation of the LMBR system a specialized Monte Carlo solution has been developed. The following are the assumptions of this simplified Monte Carlo model:

1. Particles are terminated based on user defined collision number.
2. LMBR forms images only due to Compton scatter photons.
3. Uncollimated detector images are formed by first and second collision photons.
4. Collimated detector images are formed by third and higher collision photons. The present model restricts the number of collisions to five, because the photons with collisions higher than this would not make significant energy deposition in the detectors. The collimators are not modeled in this MC model.
5. Large area detectors can be considered as regions that absorb all the energy of photons that enter these regions. The backscattered photons which do not reach these detector regions are killed.
6. The x-ray spectrum can be approximated by a monoenergetic x-ray source with equivalent energy. An equivalent energy source is a source whose energy is adjusted in such a way that the total energy deposited by this source is equal to the energy deposited by a spectral source of known energy (see Table 6-4).
7. The photon intersection cross-sections can be modeled as $\sigma = A_0 + \frac{A_1}{E} + \frac{A_2}{E^2} + \frac{A_3}{E^3}$ where A_i , $i=0 \ldots 3$, are constants. These constants are derived through least-square fit to the Burger and Hubble data.[31]

8 Implicit capture is used to reduce the number of tracked particles. Weights of the "captured" photons are biased by a factor $f=\sigma_s/(\sigma_s+\sigma_a)$, where 's' stands for scattering cross section and 'a' indicates absorption cross-section of the interacting material.

9 Any photon going 15 cm into the ground, a photon with a weight less than 0.001 or a photon with energy less than 10 eV is terminated

Table 6-4 The energy of an equivalent monoenergetic source*

Peak energy of the half-rectified spectral source (kVp)	Equivalent monoenergetic source energy (keV)
100	40.83
150	57.15
175	65.02
200	72.72

* These energies are calculated from the MCNP output which lists the mean source energy of a spectral source.

The above mentioned assumptions are used to develop a computer program, photon lateral migration simulator (PLMS). This program is structured such a way as to be amenable for parallel implementation. The flow chart of the PLMS program has already been presented as an example MC scheme in Figure 3-1. The following are the routines used in this program

Recons - Calculates the detector energy deposition for any pixel point (x,y) through the variable 'det'

Klien - Calculates the photon energy, 'E1', and the polar scatter angle,'cs' in the lab system after a Compton scatter(See Figure 3-2)

Angle - Calculates the azimuthal angles and using 'ms' generates direction cosines u,v,w for a scattered photon (see Figure 3-3).

Location - Calculates the coordinates (xx,yy,zz) after each scatter using u,v,w.

Position - using the particle coordinates (xx,yy,zz) it determines whether the particle is in mine or soil, and supplies a flag for variable 'mat' indicating the type of material (see Figure 3-4)

Weight - Implements implicit capture and applies the weight biasing factor 'f' and calculates the weight 'wei' after photon capture.

Attent - Calculates the total mass attenuation coefficient for a material 'mat' at an energy 'E'.

Attens - Calculates the incoherent scattering cross section for a material 'mat' at an energy 'E'.

Attens - Calculates the absorption cross section for a material 'mat' at an energy 'E'.

Statout - Calculates the mean and standard deviation for energy deposition for variable 'det' to be used by routine 'Recons'.

The source code of FLMS is presented as Appendix-D.

Detector model in FLMS

Collision flagging associated with this model is used to select collimated and uncollimated detectors. A detector region is defined by the raster gap size and the detector size in the raster direction along with the maximum and minimum coordinates in the motion direction. Any scattering photon that enters this region above the surface is tallied and used for image generation.

The images of 12" plastic, 12" metal and 3" metal objects buried at 1" DOB were generated through FLMS for the collimated detectors. This simulation used 90,000 particles per pixel to generate a 33 X 33 image. The results from FLMS for the front collimated detectors are presented as images in Figure 6-5.

Figure 6-5a presents the image of a 12 inch diameter plastic landmine buried at location (23,23) with 1 inch DOB. Figures 6-5 b and c show the images of a 12 inch diameter metal mine located at (16,16) and a 3 inch diameter metal mine located at (4,27), respectively. Both metal objects were buried at 1 inch DOB. An experiment was conducted by burying the above three objects in a sand box at the same locations as used in the FLMS simulation. The measured image for the front collimated detector is presented in Figure 6-6.

It can be seen from both Figure 6-5a and Figure 6-6 that the plastic mine shows a peak and this peak is shifted in the motion direction by about 4" in both the FLMS and measured images (peaks are located at (23,27)). The 12" metal object is seen as a dip in Figures 6-5b and 6-6, and there is 2.5" shift in the motion direction associated with this object. The 3" metal object is seen both in the measured and FLMS image as a small dip in the signal. The low-resolution of the 3" metal mine image can be seen in both Figure 6-5c and Figure 6-6. This shows that FLMS predicts the same trend as the actual detector signals.

PLMB simulations were also carried out to compare the single line scan results for a 1/2" per foot soil slope in the motion direction. The results are presented in Figure 6-7. The PLMB approximation is carried out with 90,000 photons per pixel. The collimated detector signals are predicted with an uncertainty of about 20% and the uncollimated detector signals are predicted with an uncertainty of 10%. The trend lines from Figure 6-6 and the trends of measured and MCNP results presented in Figure 3-14 have similar behavior, even though the uncertainties for the collimated and uncollimated detector signals in the latter case are 11% and 6%, respectively. Hence, it can be said that the images generated by the PLMB model for LMB photon transport are a good approximation of the actual images.

The PLMB collimated detector simulations took 65 minutes on a Pentium 90 MHz personal computer for generating each 33X33 image with 90,000 photons per pixel at relative uncertainty of 10% and took about 87 minutes on SPARC-20 in a multi-user mode. However on compiling PLMB with an auto-parallel option the simulation time came down by a factor of 1.8 on the SUN SPARC-20 workstation. In contrast the same calculations with MCNP (90,000 photons per pixel at relative uncertainty of 16-54) take about 6 hours on an IBM ES 9000 mainframe computer with very low mine image contrast and requires at least 200,000 particles to generate the same image contrast as PLMB. PLMB due to its collision termination feature eliminates the influence of first and second collision photons and hence produces a high contrast LMBR mine images with fewer particle histories. However, MCNP simulation does not incorporate this collision termination and hence requires higher number of particles to generate images with good contrast. Thus, it can be inferred that PLMB also aids in speedy simulation of LMB systems.

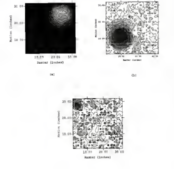

Figure 6-5 FLMS generated images for the front collimated detector, (a) the 12" plastic landmine at (23,23), (b) 12" metal mine at (10,10) and (c) 3" metal mine at (4,27). All mines are buried at 1" DOB. FLMS used 80,000 particles/pixel and the pixel intensities have uncertainty of 10%

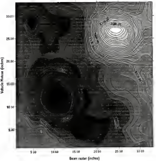

Figure 6-6 Measured front collimated detector image of a 12" diameter plastic landmine at (23,23), 12" diameter metal landmine at (10,10), and a 3" diameter metal landmine at (4,27). All mines are at 1" DOB

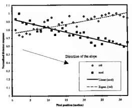

Figure 6-7 The single scan-line results from PLMS for 1/2" per foot soil slope

CHAPTER 7
LMRR IMAGE ENHANCEMENT ALGORITHMS

(Sub-pixel zooming via estimation of multiscale coefficients)

Some imaging modalities generate low-resolution images due to sampling limitation during acquisition. Additionally, region of interest images extracted from an original image may make more obvious sampling artifacts. Low-resolution images can broadly be classified as under sampled images. Wavelet based multiresolution analyses are less effective on such under sampled images because the sub-sampling associated with the standard wavelet based multiresolution algorithms reduces the capability for feature detection and analysis.[38] To overcome sub-sampling of an under sampled image, multiresolution analysis can be accomplished through an overcomplete "frame" representation and is carried out across an oversampled multiresolution frame representation. An algorithm that uses frame representations of an image obtained with an autocorrelation shell of wavelets(AsW) was implemented. An image extrapolation algorithm that uses the growth or decay of transform coefficients to generate sub-pixel information is carried out across an overcomplete multiresolution representation. The magnification procedure results in an image with very low distortion (artifacts) and outstanding presentation of contrast detail. This dissertation demonstrates the effectiveness of the algorithm on an undersampled LMRR (reflected projection) and medical x-ray images (transmitted projection).

Introduction

Imaging modalities such as lateral migration backscatter radiography (LMBR) produce low-resolution (under sampled) images. The under sampling in such imaging modalities is due to the response speed requirements of the imaging modality, and/or poor lighting condition associated with acquisition. There are situations where a region of interest selected from a high resolution image often leads to an under sampled image when magnified via traditional digital processing methods of enlargement. Features in under sampled images may not be well resolved, hence making it difficult to establish a correspondence between detected features and real objects.

Information provided by an image lies in the local variation of pixel intensity. The sudden changes in pixel intensities may appear as edges. However, in an under sampled image the discontinuity in pixel intensities is often seen as artifacts and false edges. To understand a scene, all local variations may not be important. Multiresolution analysis can provide representations of image information under various resolutions that can assist in detecting important features.[23,24] Multiresolution analyses with orthonormal wavelets (that are periodic and shift-variant) involve sub-sampling of coefficients for representing an image at lower scales. This sub-sampling is necessitated because the wavelet expansion of any vector without sub-sampling would also contain circularly shifted wavelet coefficients of the original signal. This periodic behavior of the wavelet coefficients is due to the asymmetric nature of standard wavelets used in image compression such as Daubechies wavelets.[25]

In our design, we trade off orthonormality of wavelet coefficients, for applying symmetric zero-phase wavelet filters with compact support. Such shift-invariant bases functions allow a redundant representation of images for multiresolution analysis.[26] Saito[27] has shown that an autocorrelation shell derived from a Daubechies wavelet(AoW) basis allows for such an overcomplete representation of the signal. He demonstrated the effectiveness of this algorithm for one-dimensional signals. Based on this work, we chose an AoW bases for conducting multiresolution analysis of under sampled images

From the theory of multiresolution signal decomposition, it can be said that the projection of a function f(x) at 2^j resolution leads to some loss of information. The projection of a function using any bases at resolution 2^j can thus be considered an approximation of the original function. However, as the resolution increases to $+\infty$, the image projection is no longer just an approximation of the signal but converges to the original signal. Since, the AoW representation of the signal is shift invariant, it facilitates the study of growth or decay of the image projections across resolution scales. By evaluating the trend of growth or decay of the projections of an image to an AoW domain we show how to extrapolate projection information to a next resolution scale. On the basis of AoW coefficients at lower scales, the AoW shell coefficients at a higher resolution are predicted. This leads to an automatic generation of sub-pixel information, which is used for image expansion. This chapter exposes the details of the implementation of an AoW image expansion algorithm. We then compare its results with existing state-of-the art algorithms for image extrapolation, such as pixel replication, linear interpolation, b-spline interpolation,[28] plain regularization[29] and cubic interpolation.

Background

Since the sequence of wavelet coefficients varies exponentially across scales, multiresolution analysis can be partially scale-invariant If the resolution step α is chosen such that for all integer values of j, $r_j = \alpha^j$, then the information contained in α^j is also contained in the resolution α^{j+1}. If the image details are processed using the same procedure at each resolution then the image information from a lower resolution is still retained at a higher resolution Thus, multiresolution analysis leads to representations of image information within distinct levels of resolution If we consider that the digital images are acquired by sampling a continuous image, as the resolution is increased, the information contained in the image approaches the information contained in the original continuous image Mathematically we can state this process of image approximation as

7.1 $\lim_{j\to\infty} = \bigcup_{j=-\infty}^{\infty} V_j$ is dense in $L^2(R)$

and

7.2 $\lim_{j\to-\infty} = \bigcap_{j=-\infty}^{j=\infty} V_j = \{0\}$

where V is a vector space that satisfies all the properties required for multiresolution approximations at scale j, and $L^2(R)$ is the space in which the original signal resides,

Now if we plot the V's for scales j=0, ,-n, where n is the number of discrete scales and if a trend of growth or decay of V's from scale-to-scale is established, we can predict V exactly at j=1. This estimation of V's at a higher resolution leads to generation of the sub-pixel information, Redundant or overcomplete frame representations of Vjs are useful for comparing Vj's at various scales.[23] To represent Vjs redundantly, we require Lj 's , the projection operators, to be shift-invariant and zero-phase operators Saito [24] has shown that an autocorrelation shell of Daubechies wavelets is shift invariant, and can be used to represent both a signal intensity (first derivative) and the zero-crossings (second derivatives) redundantly. Thus we can represent

Vjs redundantly and evaluate the trends of Vjs from scale-to-scale. This tracking across scales (bi-jective) allows us to carry out sub-pixel information approximation.

Implementation

The implementation of the AoW sub-pixel image information approximation algorithm is explained here through an example. Consider the image presented in Figure 7-1. This image is a low-resolution image of size(256 by 256), with a circle at the center partially covered by a rectangle. This circle has circumferential gray scale gradient and the gray levels in the rectangle change parallel to one of the diagonals. Figure 7-2 presents the amplitude of Fourier transform coefficients of a set of one-dimensional autocorrelation shell of Daubechies wavelets. The normalized periodic Fourier transformed one-dimensional AoW shell coefficients with magnitudes greater than 0.2 were truncated. This truncation is tolerated here because the AoW shell projections are used here for image analysis. It can be seen from this figure that the multi-scale representation of any signal into an AoW shell domain leads to filtering a given signal through a low-pass, a set of band-pass and a high-pass filter. The x-axis in this plot indicates the wavelet number. The level of these filters are indicated by L_n with n=0,.7, n=0 approximates a low-pass filter and n=7 approximates a high-pass filter.

The filter coefficients are generated using the following 7 coefficients, [-0.0441941, 0, 0.3977, 0.70716, 0,3977, 0, -.0441941] and [0.04491, 0, -0.3977, 0.70716, -0.3977, 0, 0.0441941] for scaling and detail functions, respectively.

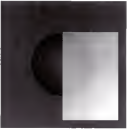

Figure 7-1 The synthetic image used for testing RoW algorithm.

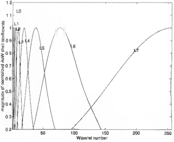

Figure 7-2 One-dimensional AoW filters in Fourier domain.

The two-dimensional filters of these 1-D signals are generated using the following approximations.

7.3 Scaling function : $\theta_n(v) = \dfrac{1}{1+\left(\dfrac{D}{D_0}\right)^{nl}}$

7.4 Detail function $\Psi_n(v) = \dfrac{1}{1+\left(\dfrac{D^2-D'_0{}^2}{DW}\right)^{nl}}$

In the above two equations,

$v=0..N$, where N is the size of the image,

D_0 is the D value at cutoff for scaling function,

D'_0 is the wavelet number at which the Fourier transform of the detailed function has the maximum amplitude,

nl is a constant complex number for a particular filter, and

W is the support of the AoW detail function.

$D = [(u-u_0)^2+(v-v_0)^2]^{1/2}$ where u_0 and v_0 are the pixel coordinates about which bases functions are symmetric and (u,v) represents a pixel position.

The amplitude of the Fourier transforms of two-dimensional AoW filters are presented in Figure 7-3. Each of these filters are of size 256 by 256 and are symmetric with respect to the image center. The generation of two-dimensional filters helps in fast implementation of the AoW multiresolution algorithm. The image in Figure 7-1 after application of these filters is presented in Figure 7-4. It can be seen from the coefficients in Figure 7-4 that as the n value increases, the image representation in L_n contains more and more image details. Additionally, the two components of this image, the circle and the rectangle can be seen as separate entities at levels L_4 and L_5 , respectively. Thus, the multiresolution analysis helps to extract features from images.

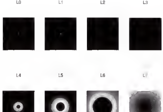

Figure 7-3 The two dimensional AoW filters in Fourier domain.

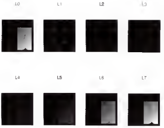

Figure 7-4 The AoW filter coefficients of the synthetic image from Figure 7-1

The log-log scale plot of the detailed filter coefficients at pixel [128,128] is presented in Figure 7-5 It is clear from this figure that a linear relationship exists between filter coefficients from scale-to-scale To verify this relationship, the coefficients at level L_0 are estimated from L_1-L_4 coefficients and the resultant image is compared with the actual level L_0 coefficients in Figure 7-6

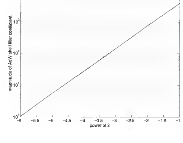

Figure 7 5 The log-log plot of filter coefficients for 32 pixels verses scale, scale is presented in powers of two

The mean squared error between these two images is 0.187 and shows that the AoW shell projection approximates the next higher level accurately.

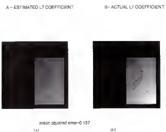

A – ESTIMATED L7 COEFFICIENT

B- ACTUAL L7 COEFFICIENT

mean squared error=0 187

(a) (b)

Figure 7-6 Comparison of estimated level L_7 filter coefficients (a) estimated level L_7 filter coefficients (b) actual AoW shell level L_7 filter coefficients for the synthetic image shown in Figure 7-5.

The above procedure is summarized in the following algorithm:

Step 0: *Determine the set of AaW shell basis functions. They are 'θ' the scaling function and ψ_j the detailed function where j denotes the scale size of the detail function*

Step 1: *Use the scaling function coefficients from step 0 and interpolate 2N points, here N is the size of the image*

Step 2: *For the scales j=0...J determine size N_j and interpolate $2N_j$ detail coefficients*

Step 3: *Fourier transform θ and ψ_j by neglecting the fold-over coefficients beyond N to obtain C, the scaling function in Fourier domain and D_j s, the detail functions in the Fourier domain.*

Step 4: *Determine D_0, D_0', W, and σi for all D_j s and C*

Step 5: *Obtain the 2-D bases using the parameters from step 4*

Step 6: *Obtain the image projections Ln in the Fourier domain with respect to each basis function through convolution of a given Fourier transformed image A with C and D_j.*

Step 7: *Apply the inverse Fourier transform on L_j and obtain a_j, the AaW shell coefficients in the spatial domain.*

Step 8: *For every pixel position, use the pixel intensities for all a_j 's, j=0...n and generate pixel values for even a_j*

Step 9: *Apply bi-linear interpolation and obtain all a_j pixel values.*

The AaW algorithm is presented schematically in Figure 7-7. The expanded image of Figure 7-1 generated using the above algorithm is presented in Figure 7-8. This image not only retains all the edges in the original

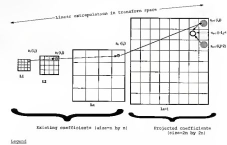
Linear extrapolation in transform space
$a_1(i,j)$
$a_2(i,j)$
$a_n(i,j)$
$a_{n+1}(i,j)$
$a_{n+1}(i-1,j+1)$
$a_{n+1}(i,j+2)$
L1
L2
Ln
Ln+1
Existing coefficients (size=n by n)
Projected coefficients (size=2n by 2n)

Legend

● Pixels generated via transform extrapolation

○ Pixels generated via bilinear interpolation

Figure 7-7 Schematic of the AoW sub-pixel estimation algorithm

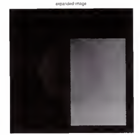

Figure 7-8 Extrapolated synthetic image from Figure 7-1.

image, but it also shows the contrast as in the original image. We can clearly see the circumferential gray scale gradient in the circle and the diagonal gradients in the rectangle. The above algorithm is implemented in Matlab.[20] To understand the effect of noise on the multiresolution analysis and the image sub-pixel information generation, three cases are studied. The first case is a zoomed portion of a Lenna image which is a 256 by 256 image, the second case is a simulated mine field image acquired through LMBR, the landmine image is a 32 by 32 image with one inch resolution and the third case is a 512 by 512 size blended mammogram.

Comparison of AoW approximation with other interpolation methods

To compare the effectiveness of AoW based image extrapolation algorithm with various other interpolation techniques, the Lenna image is considered. The original 512 by 512 image is sub-sampled to generate a 256 by 256 image. The AoW image extrapolation algorithm is applied and the 512 by 512 image is reconstructed. The extrapolated image through AoW projection algorithm is compared with the original Lenna image in Figure 7-9, and the mean squared error between these two images is 0.039. This calculation verifies that the transform based image extrapolation approximates an image in the next resolution quite accurately.

To compare this extrapolated image with other established techniques such as pixel replication, linear interpolation, cubic interpolation, pixel regularization[23] and B-spline interpolation[24] (another method of transform interpolation), these methods are applied to a zoomed portion (256 by 256) of the Lenna image. The interpolated images are compared in Figure 7-10. It is clear from this figure that

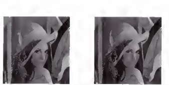

Figure 7-9 Comparison of the sub sampled and then extrapolated Lenna image with the original

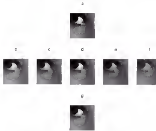

Figure 7-10 Comparison of image interpolation algorithms(a) the original (b) pixel replication (c) bi-linear interpolation (d) bi-cubic interpolation (e) pixel regularization (f) b-spline interpolation (g) AoW shell extrapolation

the cubic - interpolation gives smooth results, whereas B-spline and pixel regularization produce more dulled images. Both linear interpolation and pixel replication produce images with obvious jagged edges. The AoW approximation produces an image that is superior to cubic interpolated image with respect to sharpness. In addition, the number of operations required for the AoW algorithm is 4N compared to 6N operations required for cubic-interpolation.

Application to Landmine Detection

Landmines have been a great threat to humanity during and after a conflict; approximately 26,000 people are maimed or killed every year by landmines.[31] There are many modalities that are available for landmine detection. One such modality, LMBR, is very promising. However, the images generated through this modality are under sampled and detecting features that resemble landmines in such images is necessary for successful identification. Figure 7-11 presents an LMBR image of a simulated mine field. This mine field contains a square mine and a circular mine. It can be seen in Figure 7-11 that this mine field contains two regular shaped objects; however, it is very difficult to say that these objects are mines.

The zero-crossing representations of filter coefficients of the landmine field image is shown in Figure 7-12 after applying the AoW shell multiresolution analysis algorithm. The images at levels L_4 and L_5 show the details of a circular step pattern on the rectangular object clearly. Figure 7-13 presents the picture of the actual M-19 mine which has a similar circular feature, that provides important evidence that the rectangular object is indeed a mine. Additionally the ring patterns on the circular object is typical of many circular mines; this feature detection ability greatly assists in the identification of these LMBR

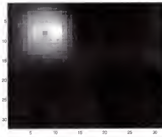

Figure 7-11 The simulated mine field image

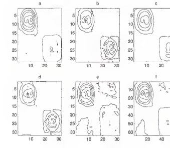

Figure 7-12 The zero-crossing representation of the A&W filter coefficients of a simulated mine field image (a) the raw image (b)L_0(c)L_1(d)L_2(e)L_3(f)L_4

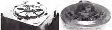

Figure 7-13 The M-19 mine and typical cylindrical mines.

[illegible] as shown. A sub pixel approximation of the simulated mine field image is presented in Figure 7-14. Note that this image retains all the edge information associated with the original image while improving the contrast. This example demonstrates the effectiveness of AaW shell algorithm for multiresolution analysis of an under sampled image

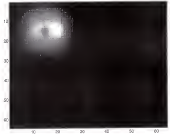

Figure 7-14 Sub-pixel expanded (4X) mine field image

Application to Mammography

Typical mammograms are high resolution images of size 1024 by 1024 pixels. Detecting features in mammograms plays an important role in diagnosis of breast cancer. However, zoomed regions of these mammograms result in a under sampled image. To test the effectiveness of AoW shell algorithm in enhancing features in mammograms, a 512 by 512 mammogram with blended phantoms is considered as a test example. These phantoms represent micro-calcifications, speculation and mass. Figure 7-15 presents a 256 by 256 size undersampled version of this mammogram. The cropped image presented in Figure 7-15b shows that undersampling results in loss of details. The AoW shell image extrapolation algorithm is applied to this image. The region-of-interest is cropped from the extrapolated image and is compared with the same region in the original 512 by 512 image in Figure 7-16. The original 512 by 512 and the transform extrapolated image are also presented in the same figure. It can be seen from this figure that the AoW shell transform expansion algorithm produces a good approximation of the original image and retains all the features in the original image except that one of the spokes in the star pattern is jagged. This is due to the loss of information during sub-sampling and is evident from Figure 7-15(b). The presence of a star pattern not very clear in the image presented in Figure 7-15(b). However, the presence star pattern is detectable in Figure 7-16(d). This study demonstrates how a AoW shell extrapolation algorithm can support pattern recognition algorithms.

Summary

The redundant representation of an wavelet transform coefficients of an image computed from autocorrelation shell of an wavelet can support reliable multiresolution analysis of under sampled images On the statistical basis of the trend of AcW coefficients at each pixel, sub-pixel information is approximated at a higher resolution. The quality of an image expanded through the transform-based AcW shell algorithm is comparable to or exceeds the quality of an image expanded through a cubic image interpolation algorithm at reduced computational cost(33% faster) Thus, the AcW algorithm provides a strong mathematical framework for carrying out multiresolution analysis and image magnification for under sampled images

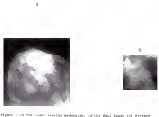

Figure 7-15 The under sampled mammogram, (a)the full image (b) cropped region

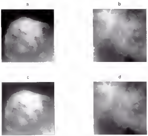

Figure 7-16 The comparison of the extrapolated image with the original mammogram along with a comparison of a region of interest(a) the original 512 X 512 image (b) the zoomed portion of the original image (c) the sub-pixel information generated using sub-sampled version from 7-15(e), (d) the zoomed portion of the image in (c).

CHAPTER 8
SUMMARY AND CONCLUSIONS

This dissertation not only studies the phenomenon of lateral migration backscatter but it also demonstrates the capability of the Monte Carlo technique for designing imaging systems such as LMBR. Additionally, this dissertation develops the methodology for designing LMBR systems and enhancing LMBR images. Though the LMBR system studied here is a landmine detection system, the tools developed in this research can be used for development of other LMBR applications. This chapter briefly summarizes the findings of this dissertation.

1. The Monte Carlo method of simulating photon transport, specifically MCNP, has been found suitable for simulating photon and electron-photon transport. The random number generator used in MCNP is found adequate for the simulation of photon and electron-photon transport in a LMBR system. The predicted results from MCNP are within 10% of the measurements for the photon transport simulations. The difference between MCNP results and measurements for the electron-photon transport problems is as great as 50%. This difference is due to the idealization of a complex electron source in the MCNP simulations. Additionally, MCNP does not consider long range e-e forces in its treatment of electron transport.
2. A LMBR based landmine imaging systme has been analyzed using MCNP/SABRINA. This analysis revealed that materials with lower electron density (low Z and low density) allow higher lateral migration of the third and higher collision photons. High migration

lengths in low electron density materials leads to creation of a large diameter 2π disc secondary source in a scattering material. The multiple collision photons from this disc source predominantly form images of sub-surface or buried objects but also retain the first-collision source distribution as a major component. A large area collimated detector can be optimally designed to predominantly image these multiple-scatter photons. The effectiveness of such a collimated detector design has been demonstrated for a LMBR-landmine detection system.

3. The uncollimated detectors detect predominantly the first and second collision photons and image surface or near surface features. A LMBR system using collimated and uncollimated detectors is capable of generating two images one containing predominately surface features and the other containing both surface and buried features. These images provide a means for removing the influence of first-scatter photons from the images of buried objects.
4. The combination of uncollimated and collimated detector images helps in discriminating low-Z, low density materials from low-Z higher density materials. This improves the ability to distinguish plastic explosive from soil, wood, and vegetation. The photon lateral migration length is different for each material. The difference in lateral migration length leads to unique signatures for different materials in uncollimated and collimated detector image sets. These signatures can be used to approximately determine the material of the imaged object. This feature discrimination capability of LMBR is demonstrated by the success of LMBR in differentiating plastic from

metal landmines, wooden disks from landmines, and pot-holes from landmines

5 The one-dimensional x-ray spectrum prediction code XSPEC has been developed and its results compared with measurements from a Maxitron-300 x-ray source. The trends of the results from the XSPEC code agree with measurements within a factor of 20-40% for 100, 150 and 200 kVp spectra. The MCNP simulations of the Maxitron-300 x-ray spectra have shown that the detailed three dimensional simulation of the x-ray source in MCNP provides more accurate results than XSPEC and the MCNP predictions agree within a factor of 20-30% of measurements for 100,150 and 200 kVp spectra. These analyses demonstrate the suitability of XSPEC and MCNP for modeling x-ray generators for LMBR systems. At energies higher than 150 kVp, the fast running XSPEC can be used to approximate x-ray spectra instead of MCNP.

6 On the basis of the MCNP/SABRINA analysis of LMBR systems, two approximate solutions to the transport phenomenon governing the photon lateral migration backscatter have been developed.

(a) The first method uses a deterministic two-collision model with a stochastic treatment for calculating the first and second scattering angles. The two-collision algorithm has been tested for predicting mine parameters from LMBR landmine images. The two-collision model predicts mine parameters within 10% of the actual parameters for the examined configurations. A cylindrical landmine image restored using a two-collision model with stochastic scattering angle calculation is circular and smoother than the image restored by a two collision model using two 90 degree scatters.

(b) The second approximation method is a simplified collision-based Monte Carlo approximation of the photon lateral migration backscatter phenomenon. This approximation leads to a fast running photon lateral migration simulator(PLMS)-an LMBR simulation algorithm. The PLMS images and single-scan lines show similar features to the measured images. PLMS can be used as a tool for checking the suitability of LMBR for imaging object discontinuities.

7. The redundant representation of an wavelet transform coefficients of an image computed from autocorrelation shell of an wavelet can support reliable multiresolution analysis of under sampled images. On the statistical basis of the trend of AoW coefficients at each pixel, sub-pixel information is approximated at a higher resolution. The quality of an image expanded through the transform-based AoW shell algorithm is comparable to or exceeds the quality of an image expanded through a cubic image interpolation algorithm at reduced computational cost(33% faster). Thus, the AoW algorithm provides a strong mathematical framework for carrying out multiresolution analysis and image magnification for under sampled images.

From these results it can be concluded that the basis for establishing the theory dictating a new imaging modality, LMBR has been developed along with a new transform based approach to the two-dimensional interpolation problem. Based on the theory and methodology developed here, many applications of LMBR and transform based image extrapolation can be developed.

The following are conclusions/limitations of this research work:

1. The LMBR landmine imaging system developed here can be used to image buried plastic landmines to a depth of less than four inches. Beyond this depth, the signal from the soil overwhelms the signal from the mine and will substantially reduce the MSR. Increasing the source energy will not solve this problem because even though these high energy incident photons penetrate to a greater depths in the soil, they will also undergo more first-collisions in the soil. These first collision photons reduce the contrast due to mine information carried by the multiple-collision photons and, hence, images cannot be generated with sufficiently high MSR. However, most landmines are buried shallow (to a depth of about two to three inches) and can be imaged with LMBR. If the atomic number of a buried object is far greater than the atomic number of the background, increasing the energy of the incident photons will improve the signal-to-noise ratio and LMBR can be applied to image high Z objects for DOBs greater than four inches.
2. The Monte Carlo LMBR analysis presented here studies only the multiple-collision photons in the energy range of interest to landmine imaging and cannot be generalized to photons of all energies.
3. The mine detectability is defined here based on MSR. However, to determine the threshold MSR, a receiver operating characteristic(ROC) experiment has to be conducted using the acquired landmine images. A ROC experiment uses the true-positives and false-positives for landmine detection to determine the threshold MSR above which the true-positives are maximized while false-positives are minimized.

4. The two-collision model developed here is very specific to cylindrical plastic objects; its applicability to other scattering materials has to be verified. Additionally, a two-collision kernel along with image subtraction can be used for correcting the multiple-scatter photon effects in other scatter radiography techniques.
5. PLMS unlike MCNP includes the collision termination feature. This particle termination efficiently eliminates the influence of first and second-collision photons from LMBR images and hence produces an excellent image contrast with fewer particle histories. For example, the contrast in PLMS generated images with 90,000 particles/pixel is comparable to the contrast in MCNP generated images with 200,000 particles/pixel. The PLMS program is limited to the simulation of large area detectors. With appropriate changes to detector geometry, the PLMS program can be used for simulating other scatter radiography applications. The use of pseudo-particles and deterministic estimates like point detectors can be included to improve PLMS. Additionally, PLMS is now limited to two-cell problems and has to be extended to multiple cells for conducting multiple object LMBR image generation.

Future developments

The following are recommendations for future research:

1. The MCNP results obtained for the electron-photon transport problem are not very close to the measured results. It is suggested that a simplified experiment with a well-defined electron source (example: β source) and target bremsstrahlung generation be conducted. The experimental setup can then be simulated in MCNP and the

bremsstrahlung photon flux tallied to accurately determine errors associated with the modeling x-ray spectra with MCNP. Because MCNP does not consider the electric and magnetic field effects, it is recommended that a coupled electron-photon Monte Carlo transport program such as the ITS-TIGER[37] series which considers the above two effects be used. The electron transport with e-s and e-m fields plays an important role in the modeling of x-ray generators and its validation will improve the reliability of Monte Carlo based x-ray generator design.

2. Extend LMBR to lateral migration forward radiography (LMFR). In LMFR, the detectors are placed so as to detect multiple-collision forward scattered photons. This detector arrangement can reduce the source strength requirement and enable the use of conventional x-ray sources for some radiography applications. However, this modality would be limited to imaging objects that are accessible from two opposite sides. The LMFR can work as an useful tool for non-destructive examination of industrial components, especially composites made of low Z materials.
3. An artificial intelligence(AI) algorithm to discriminate different objects in LMBR images can be developed. The AI algorithm can use some of the signatures in LMBR images to differentiate various objects and can be trained through a set of MCNP or PLMS simulated images. This AI algorithm would enlarge the scope of LMBR for other detection applications.
4. The multiresolution feature enhancement algorithm presented in chapter 7 is in dyadic scales and can be extended to integer scales to improve its feature extraction capabilities. This algorithm can be

integrated with an image segmentation algorithm to facilitate the anomaly detection capability of the image segmentation algorithms.

5. Apply quasi-random methods for simulating photon transport in the PLMS program. This approach is expected to speed up the convergence of solution. Solutions using quasi-random methods are known to converge as $1/N$ as against $1/N^{1/2}$ for Monte Carlo, where N is the number of samples. The quasi-random methods use Halton series instead of pseudo-random numbers to implement numerical integration

APPENDIX A
THE MONTE CARLO SOLUTION TO THE BOLTZMANN TRANSPORT EQUATION

For the solution of the photon transport problem, the MC technique can consider either the integral or integro-differential form of the BTE or neither. The selection of the form of the BTE is entirely dependent on the problem. The integral form of the BTE will be considered here because the MC solution to the BTE in this form is straight forward compared to the intergro-differential equation approach.[11] The integral form of the BTE is given by

A 1 $F(R) = \int K(R{:}R')F(R')dR' + S_f(R)$

where

$S_f(R)$= the first flight collision density due to an external source at R,

F(R)= collision density at R,

F(R')= collision density at R', and

K(R:R') = next flight collision density at R due to collision density at R'.

The kernel K(R:R') is given by

A 2 $K(R{:}R') = [1-\alpha(R')] * \eta(R') * \beta(R{:}R')$

where

α(R') is the capture probability at R',

η(R') is the normalization factor, and

β(R:R')= normalized kernel for the collision density at R due to a collision at R'.

For multiple collision photon transport, the collision density can be written as

A.3 $$F(R) = \sum_{0}^{\infty} \int S_c(R_0)K(R_0 : R_1)K(R_1 : R_2) \ldots K(R, R_{n-1})dR_0 dR_1 \ldots dR_{n-1}$$

The purpose of the MC method is to compute measurable quantities such as flux, energy deposition, etc. Since most of these measurable quantities are linearly proportional to the collision density, we can define a functional that defines these measurable quantities. These functionals can be generally described by

A.4 $$W(R_0 \ldots R_n) = \frac{h(R_n)}{\alpha(R_n)} \prod_{i=0}^{n-1} \eta(R_i)$$

where h(R) is the contribution that collision at R makes to the functional of interest

A.5 $$J = \int F(R)h(R)dR$$

Using equations A.2, A.3 and A.4, equation A.5 for a multi-collision process can now be written as

A.6

$$J = \sum_{0}^{\infty} \int \ldots \int S_c(R_0)[1 - \alpha(R_0)]\beta(R_1 : R_0)[1 - \alpha(R_1)]\beta(R_2 : R_1)[1 - \alpha(R_{n-1})]\beta(R_n, R_{n-1})\alpha(R_n)W(R_0, \ldots R_n) \ldots dR_0 dR_1$$

This expansion is used to construct the MC solution to the photon transport problem. Physically, the above equation indicates a process starting from a point R_0 with a first collision density distribution $S_c(R_0)$ with α representing the termination of the photon at any R and β(Ri:Ri-1) is the collision density kernel at R_i due a collision at R_{i-1}. Continuing the same process for the phase volume dR_i about R_i and terminating the chain at the n+1 st collision, we can model the photon transport. The above equation can now be written as an expectation value of weights W, i.e.,

A.7 $$J = E[W]$$

Equation A 7 has a drawback in that it breaks down when the capture or scattering cross section for a given material becomes zero. To overcome this problem, some fictitious capture or scattering cross-section is assumed at that point and the photon weight W is suitably adjusted to $\tilde{W}$ so that equation A 7 becomes

A 8 $\quad J = E(\tilde{W})$

The above discussion shows that the integral transport equation for the photon transport can be solved by the MC technique

APPENDIX B
CALCULATION OF AVERAGE ENERGY AND ANGLES FOR COMPTON SCATTER

The following equations are used to calculate the average scattering angle and energy for the first-collision Compton scattered photons. Let us define a weighting function f, that defines the K-N differential cross section

$$\text{B 1} \quad f = r_0^2\left[\frac{1}{1+\alpha(1-\cos\theta)}\right]^2\left(\frac{1+(\cos\theta)^2}{2}\right)\left(1+\alpha^2\frac{(1-\cos\theta)^2}{(1+(\cos\theta)^2)(1+\alpha(1-\cos\theta))}\right)$$

where $\alpha = E/511$; E is the photon energy in keV, r_0 is the classical electron radius

Using the above factor 'f' , the total cross section is calculated from

$$\text{B 2} \quad \sigma_t = \int_0^{\pi} 2.\pi \sin\theta . f. d\theta$$

The average forward scattering cross section is obtained through

$$\text{B 3} \quad \sigma_f = \int_0^{\frac{\pi}{2}} 2.\pi \sin\theta . f. d\theta$$

The average backscattering cross section is obtained from

$$\text{B 4} \quad \sigma_b = \sigma_t - \sigma_f$$

The average forward and backward scattering angles are calculated as follows:

$$\text{B 5} \quad \cos\theta_f = \frac{1}{\sigma_f}\int_0^{\frac{\pi}{2}} 2\pi \sin\theta . \cos\theta . f. d\theta \text{ and}$$

B6 $\cos\theta_- = \frac{1}{\sigma_-}\int_{\frac{\pi}{2}}^{\pi} 2\pi \sin\theta . \cos\theta . f . d\theta$

The average forward and backscattered photon energies are calculated as

B7

$$E_+ = \frac{\int_0^{\frac{\pi}{2}} 2.\pi.\sin\theta.f.\left(\frac{E}{1+\alpha(1-\cos\theta)}\right)d\theta}{\int_0^{\pi/2} 2\pi \sin\theta . f \; d\theta} = \frac{\int_0^{\frac{\pi}{2}} 2.\pi.\sin\theta.f.\left(\frac{E}{1+\alpha(1-\cos\theta)}\right)d\theta}{\sigma_+}$$

and

B8

$$E_- = \frac{\int_{\frac{\pi}{2}}^{\pi} 2.\pi \sin\theta.f.\left(\frac{E}{1+\alpha(1-\cos\theta)}\right)d\theta}{\int_{\pi/2}^{\pi} 2.\pi.\sin\theta.fd\theta} = \frac{\int_{\frac{\pi}{2}}^{\pi} 2.\pi.\sin\theta.f.\left(\frac{E}{1+\alpha(1-\cos\theta)}\right)d\theta}{\sigma_-}$$

APPENDIX C

XSPEC: THE X-RAY SPECTRA SIMULATION PROGRAM

```
c*****************XSPEC********************************************
c       developed by shyam p keshavamurthy based on
c       program to calculate the x-ray spectra from tungsten
c      uses the equations from D Tan and E Newton Appl. Rad
c      isotopes vol45, No11, pp 1101-1111,1994 and the characteristic
c      x ray production is calculated based on the article
c      Tucker, Barnes and Chakraborthy, Med. physics 18(2), Mar/Apr 1991
c      defines some of the constants used in this program
c      This program uses electron transport through thick targets
c******************************************************************
      implicit real*8 (A-H,o-z)
      real*8 En(3000),Im(3000),Int1,int2,meu,pi, e_dip(3000),vz(100)
      real*8 fkv(100)
      dimension flen(10)
c     The Charecteristic X ray energies for Tungsten
         E1= 57.98
         E2= 59.32
         E3= 67.15
         E4= 67.20
         pi=3.1415
      write(*,*)"***Please give the type of voltage***"
      write(*,*)"*************Flag for D.C<1*******************"
      write(*,*)"************Flag for half-rectified>1*************"
      write(*,*)"Flag="
      read(*,*)flag
      write(*,*)"please give the number of filters"
      write(*,*)
      read(*,*) filnum
      do ifl=1,filnum
c    read the filter thickness for n-filters
            read(*,*)flen(ifl)
      end do
      if (flag.le.1) then
c ***********D C Source*********************************************
      write(*,*)"output file is 'xspec.out'"
      open(8,file='xspec.inp')
      open(9,file='xspec.out')
      read(8,*)A,Z,U,ang,angr
c     NN is the number of divisions in the energy spectrum
      del=1.0
      NN=int(U/del)
      E=0.5*del
      del1=0.5
      del2=del1*2.0
      do i=1,NN
        en(i)=E
c     /***calculates the bremsstralung spectrum ***/
        call brstral(E,U,Z,A,ang,angr,in1)
c     /***Calculation of the characteristic X-ray ***/
            eps1=(E-E1)
            eps2=(E-E2)
            eps3=(E-E3)
            eps4=(E-E4)
            if((abs(eps1).ge.del1).and.(abs(eps1).lt.del2)) then
            f=.2572
            Ek=E1
            call ch_xray(U,E,A,ang,angr,Ek,f,in2)
            elseif((abs(eps2).ge.del1).and.(abs(eps2).lt.del2))then
```

```
               f=.45
               Ek=E2
               call ch_xray(U,E,A,ang,angr,Ek,f,in2)
               elseif((abs(eps3).ge.del1).and.(abs(eps3).lt.del2))then
               f=.0387
               Ek=E3
               call ch_xray(U,E,A,ang,angr,Ek,f,in2)
               elseif((abs(eps4).ge.del1).and.(abs(eps4).lt.del2))then
               f=.1521
               Ek=E4
               call ch_xray(U,E,A,ang,angr,Ek,f,in2)
               else
               endif

             in(i)=(in1/e+in2)
c
c    /*** calculates the attenuation through Al Filters***/
              call attenBe(meu,E)
              in(i)=in(i)*exp(-meu*.45)
              call attenAl(meu,E)
              do ifl=1,filnum
                in(i)=in(i)*exp(-meu*flen(ifl))
              end do
c /**** calculates the flux at 1 meter*********/
               in(i)=in(i)/(4*pi*100.0**2)
              e=E+del
              in1=0.0
              in2=0.0
              meu=0.0
          end do
c************half-wave rectified source*********************************
        else
         write(*,*)'output file is 'enspec.out''
        open(2,file='mxspec.inp')
        open(3,file='enspec.out')
        read(2,*)A,U,ang,angr
c       NN is the number of divisions in the energy spectrum
        del=2
        del1=1.0
        del2=del1*2.0
        NN=int(U/del)
        E=0.0
c       calculates the applied voletage for 20 sample points****
        do kv=-10,10
                ikv=ikv+1
                vz(ikv)=(U*cos(pi*kv/20))

                fkv(ikv)=0.125

                end do
          ikv=1.0
                fkv(1)=0.03125
                fkv(2)=0.0625
                fkv(9)=fkv(2)
                fkv(10)= fkv(1)
             do i=1,NN
               en(i)=E
               do jj=1,20
                 epsvz=E-vz(ikv)
              if(epsvz.ge.del)then
c       /***calculates the bremsstrelung spectrum ***/
              call bretrel(E,U,E,A,ang,angr,in1)
c       /***Calculation of the characteristic X-ray ***/
              eps1=(E-E1)
              eps2=(E-E2)
              eps3=(E-E3)
              eps4=(E-E4)
         if((abs(eps1) ge del1).and (abs(eps1) lt del2)) then
         f=.2572
         Ek=E1
         call ch_xray(U,Z,A,ang,angr,Ek,f,in2)
         elseif((abs(eps2) ge del1).and (abs(eps2) lt del2))then
         f=.45
         Ek=E2
         call ch_xray(U,Z,A,ang,angr,Ek,f,in2)
         elseif((abs(eps3) ge del1).and (abs(eps3) lt del2))then
         f=.0387
         Ek=E3
         call ch_xray(U,Z,A,ang,angr,Ek,f,in2)
         elseif((abs(eps4) ge del1).and (abs(eps4) lt del2))then
         f=.1521
         Ek=E4
         call ch_xray(U,Z,A,ang,angr,Ek,f,in2)
         else
         endif
c*********completes calculation of characteristic x-rays**************
         in(l)=in(l)+(in1/e+in2)
c      /** calculates the attenuation through Be window**/
         else
         endif
         in1=0.0
         in2=0.0
         lkv=lkv+1.0
         end do
         call attenBe(meu,E)
         in(l)=in(l)*exp(-meu*.45)
c   /*** calculates the attenuation through Al Filters***/
         call attenAl(meu,E)
         do lfl=1,flnum
          in(l)=in(l)*exp(-meu*flen(lfl))
        end do
          in(l)=in(l)/(4*pi*30.0**2)
         e=E+del
       end do
     endif
    do j=1,NN

       e_dip(j)=en(j)*in(j)
       in(j)=in(j)/j
100 format(x,F10.5,2x,E12.5)
       tot_eng=tot_eng+e_dip(j)
       xin=xin+in(j)
       write(8,100)en(j),in(j)
    enddo
   stop
   end
c***************************************************************
    Subroutine brstrl(E,U,Z,A,ang,angr,In1)
c Calculated the bremsstrahlung spectra
   implicit real*8 (A-H,o-z)
    real*8 in1,in1x,meu,Nm
    nnum=5
    Jmax=20
    eps=1.e-6
    est=-1.e30
    es=-1.e30
    Nm=4.73e14/511.0
    pi=3.1415
    Dens=19.3
    Amsp=202.41
    Bmsp=1036.10
    Cmsp=7.04695
    A0=3.605D-2
    A1=2.800D-5
```

```
        B1=-0.048
        B2=10.047
        B3=-10.516
        B4=3.042
        inl=0.0
        theta=ang*pi/180.0
        thetar=angr*pi/180.0
        c=0.0286*(Z/A)**2.5
        sig0=Km*Z**2/A
         do jm=1,jmax
                   inlx=0.0
                   del=(U-E)/(nnum)
             t=E+0.5*del
             Call attenuW(mau,t)
            do j=1,nnum
      B=(A0+A1*U)*(1+(B1*U/t)+B2*(U/t)**2+B3*(U/t)**3+B4*(U/t)**4)
            F=exp(-mau*(U**2-t**2)*cos(theta)/(dens*c*cos(thetar)))
            Atc=Amsp+Bmsp*exp(-t*Cmsp)
            sum=sum+(B/Atc)*F*sig0/t
            t=t+del
             enddo
             inlx=0.5*(U-E)*sum/nnum
             inl=(4*inlx-ost)/3.0
            if(abs(inl-os).lt.eps*abs(os)) return
            os=inl
            ost=inlx
        enddo
        return
        end
c*************************************************************
        subroutine ch_xray(U,Z,A,ang,angr,Ek,f,in2)
        implicit real*8 (A-H,O-Z)
        real*8 inl,in2x,meu,Km,sum
        nnn=5
        Jmax=20
        eps=1.e-6
        ost=-1.e30
        os=-1.e30
        sum=0.0
        Pi=3.145
        Km=4.73E14
        Ak= 1.349E-3
        nk= 1.648
        theta=ang*pi/180.0
        thetar=ang*pi/180.0
        c=0.0286*(Z/A)**2.5
        sig0=Km*Z**2/A
        Call attenuW(meu,Ek)
          do jm=1,Jmax
                   in2x=0.0
                   R=(U**2-Ek**2)/(19.3*c)
                   del=R/nnn
                   x=0.5*del
                   do j =1,nnn
               xp=3.0/2.0*(1-(x/R)**2)
                     sum=sum+xp*Ak*((U/Ek-1)**nk)*f*xp*exp(-
                         meu*x*cos(theta)/(cos(thetar)))*sig0
                         x=x+del
            end do
            in2x=0.5*R*sum/(nnn)
            in2=(4*in2x-ost)/3.0
            if(abs(in2-os).lt.eps*abs(os)) return
            os=in2
            ost=in2x
          enddo
        return
        end
```

```
c  ***********************************************************************
        subroutine attenW(emu,e)
c       subroutine that calculates attenuation coefficient in
c       tungsten
         implicit real*8 (A-H,o-z)
         real*8 emu, a(10)
          if(e.lt. 88.50) then
              a(1)=2.394E-2
              a(2)=-3.401E-2
              a(3)=1.623E-1
              a(4)=-4.745E-3
              a(5)=1.318E-4
         else
             a(1)=4.312E-2
             a(2)=-3.636E-1
             a(3)=1.485
             a(4)=-8.484E-1
             a(5)=2.384E-1
        endif
        u=e/100.0
        emu=a(1)+a(2)/u**1.6+a(3)/u**2.7+a(4)/u**3.5+a(5)/u**4.5
        emu=emu*19.3
        return
        end
c ************************************************************************
        subroutine attenAl(emu,e)
c       subroutine that calculates attenuation coefficient in
c       tungsten
         implicit real*8 (A-H,o-z)
         real*8 emu, a(10)
           a(1)=8.88E-3
           a(2)=8.76E-3
           a(3)=-5.653E-3
           a(4)=3.531E-3
           a(5)=-2.466E-4
        u=e/100.0
        emu=a(1)+a(2)/u**1.6+a(3)/u**2.7+a(4)/u**3.5+a(5)/u**4.5
             if (emu.le.0.0) then
                    emu=1.0
             else
             endif
        emu=emu*2.7

        return
        end
c*************************************************************************
        subroutine attenBe(emu,e)
c       subroutine that calculates attenuation coefficient in
c       beryllium
         implicit real*8 (A-H,o-z)
         real*8 emu, a(10)
         a(1)=766.8754
         a(2)=-40.4897
         a(3)=3.8935
         a(4)=0.0848
         emu=a(1)/e**3+a(2)/e**2+a(3)/e+a(4)
             if (emu.lt.0.0) then
                    emu=1.0
             else
             endif
             emu=emu*1.8
        return
        end
```

APPENDIX B
THE PROGRAM PLMS

```
c*****************************************************************
cPROGRAM PLMS
c     This program produces CS images using Monte_Carlo technique
c     some constant values have to be changed to account for actual c
       positions
c     Developed by Shyam keshavmurthy
c     6-15-95 first version
c     9-29-95 the ismate routine was added
c     12-14-95*****still improved
c     12-28-95***detector geometry is introduced
c     following subroutines and subprograms are used
c     klien -returns the scattered energy and angle
c     angles - gives the direction cosines
c     position-determines the position of the particle
c     location -gives the co-ordinates of the scattered photns
c     attenu -gives the attenuation coeffecient of the material mat
c     scatout-subroutine that gives the output
c     weight subroutine that adjusts the weight of the particles as they
c             interact


c*****************************************************************

        implicit double precision (a-h,o-z)
        parameter(em=5)

        dimension x(2),e(em)
        integer it,it1 tim
        common c(5)
c*****this program generates the plastic mine image
        open(5 file='xx dat')
        call timer(it)
        open(6 file= img img')
        read(5,*)(e(i),i=1,5)
        read(5,*)c(1),C(5),npmax,kcol
c        e(1)=DOB
c        e(2)=Mine Height
c        e(3)=Radius
c        e(4)=x location
c        e(5)=y-location
c         c(1)=signal with no-mine
c         c(5)=half the center gap

        do i=1,32
          do j=1,32
                x(1)=i
                x(2)=j
                call fresp3(x,e,y,em,npmax,kcol)
                write(5 *)x(1) x(2) y
                end do
         end do
        call timer(it1)
        tim=it1-it
        write(6 *)'time for this run is' tim
        stop
        end
c*****************************************************************

       subroutine fresp3(x,e,y,em npmax kcol)
       implicit double precision (a-h,o-z)
       dimension x(2),e(em)
```

```
      common/iocam/xm0,ym0,h,R,h1,xm0,zl
      common c(8)

      xm0=12.0

         zl=c(5)
         dei=1.0
         det=0.0
         ix=x(1)
         iy=x(2)
         xm0=e(4)
         ym0=e(5)
         r=a(3)
         h1=a(2)
         h=a(1)
c****calculate the collision response***************
         call recons(ix,iy,det,sdet,npmax,kcol)

         y=det*c(1)
c****calculate the derivatives***********************

       return
       end
c*****************************************************************
cHERE WE START THE MONTE CARLO CALCULATION************************
c****recons gives the planar detector response********************
c*****************************************************************
      subroutine recons(ix,iy,det,sdet,npmax,kcol)
c     some of the flags used in this program are
c     ternat -terminates the particle calculation
c     himine  particle which interacts with the mine
c     ALL UNITS ARE IN inches
      implicit double precision (a-h,o-z)
      common/iocam/xm0,ym0,h,R,h1,xm0,zl
      dimension x(Npmax),y(Npmax),e(Npmax),emt(Npmax),dep(Npmax)
      dimension sx(npmax),sy(npmax)
      common/rando/grand
      dens=1.0
      ei=0.0
      dete=0.0
      detm=0.0
c****START THE ACTUAL CALCULATION*********************************

      do ip=1,Npmax
      grand=5.0
      u0=0.0
      v0=0.0
      w0=1.0
         mat=2
         e=100.0
         wei=1.0
         x(ip)=ix
         y(ip)=iy
         call attent(e,mat,sigt)
         e(ip)=12.0-log(ran3(grand))/(sigt*dens)

         sx(ip)=ix
         sy(ip)=iy
            ic=0
            ternat=0
            dep(ip)=0.0

                  do while(ternat.lt.1)
                     el=e/511.0

                    call klein(el,eli,cs)
                    el=el1*511.0
```

```
                       if(el.lt.10.0)ternat=1
                       e=el
                 call angles(u0,v0,w0,cs,cdelta,sdelta,u,v,w)

                 call locatime(x,y,z,u,v,w,e,mat,ip,Npmax)
                 u0=u
                 v0=v
                 w0=w

                        call posltime(x,y,z,mat,ip,Npmax)
                        call weight(mat,e,wel)

                               if(mat(ip).ne.1) then
                                       mec(ip)=mat
                               else
                               endif
                        ic=ic+1
c   ************ PARTICLE TERMINATION**************
                        if(ic.gt.kcol)ternat=1.0
                        if(abs(x(ip)).gt.60.0)ternat=1.0
                        if(abs(y(ip)).gt.60.0)ternat=1.0
                        if(r(ip).gt.30.0)ternat=1.0
                        if(wel.lt.1E-4)ternat=1.0
c*****************************************************
                  end do
              dep(ip)=e*wel
                ly=(sy(ip)-y(ip))
                       if(ly.ge.zl)then
c***************here 12 is the ground height from the source
                               if(r(ip).lt.12.0)then
                                       sl=sl+1.0
                                       det=det+dep(ip)/npmax
                               if(mat(ip).lt.2.0) then
                                       detm=detm+dep(ip)/npmax
                               else
                                        dets=dets+dep(ip)/npmax
                               endif
                 else
                 endif
           else
           endif
      end do
      det=det/sl
      call statout(x,y,r,sx,sy,mat,dep,Npmax,det,zl,sdet)



      return
      end
c*************************************************************************
      subroutine klein(e1,e2,cs)
c        sample the klein-nishina distribution
c        e1 = energy in   e2 = energy out   cs = scattering cosine.
c        the unit of energy is the rest mass of the electron.
c        reference  r. n. blomquist and e. m. gelbard  nuclear science
c        and engineering  83, 380-384 (1983)
c     this routine is from MCNP programe
      implicit double precision (a-h,o-z)
      common/rqund/qrand
c

      a=1./e1
      b=1./(1.+2.*e1)
c
c        kahn's method (e < 1.5 mev) aecu-3258
      if(e1.ge.3.)go to 30
      t=1./(1.+8.*b(

   10 if(ran3(grand) le t(go to 20
      s=(1 +2 *el*ran3(grand))*b
      cs=1.+s*(1.-1./s(
      if(ran3(grand) gt .5*(cs**2+s((go to 10
      el1=el*s
      return
   20 r=2 *ran3(grand)
      s=1./(1.+el*r(
      if(ran3(grand) gt 4.*s*(1.-s))go to 10
      el1=el*s
      cs=1 -r
      return
c
c        koblinger's method (e > 1.5 mev( nse 56,218(1975)
   30 t=ran3(grand)*(4 *s+ 5*(1.-b**2(-(1.-2 *(1 +el(*e**2(*log(b((

      if(t gt 2 *e)go to 40
      r=2 *ran3(grand(
      cs=1 -r
      el1=1 /(e+r(
      return
   40 if(t gt 4 *e)go to 50
      el1=el*(1.+ran3(grand)*(b-1.((
      cs=1 +e-1 /el1
      return
   50 if(t gt 4 *e+ 5*(1 -b**2))go to 60
      el1=el*sqrt(1 -ran3(grand(*(1 -b**2((
      cs=1.+e-1./el1
      return
   60 el1=el*b**ran3(grand(
      cs=1.+e-1./el1
      return
      end

c*********************************************************************
      subroutine angles(u0,v0,w0,cs cdelta,sdelta,u,v,w)
c     Calculates the scattering angles of the photon
c     meu-scattering angle in lab system
c     cdelta=cosine of the azymuthal angle
c     sdelta=sine of the azymuthal angle
      implicit double precision (a-h,o-z(
      common/rando/grand
      c3=2.0
      do while(c3 gt 1.0(

            r1=ran3(grand(
            c1=2*r1-1.0

            r2=ran3(grand)
            c2=2*r2-1.0
            c3=c1**2+c2**2
      enddo
      c4=c3**0.5
      sdelta=c1/c4
      cdelta=c2/c4
      call angle1(u0,v0,w0,u,v,w,sdelta,cdelta,cs(


      return
      end
c*************************************************************
      subroutine angle1(u0,v0,w0,u,v,w,cdelta,sdelta,cs(
      implicit double precision (a-h,o-z)
      common/rando/grand
      c5=(1.0-cs**2)**0.5
      tem=0.99999-abs(w0)
          if(tem.lt.0)then
                      u= c5*cdelta
                      v= c5*sdelta
                      w=cs*w0/abs(w0)
          else
                      c6=(1.0-w0**2)**0.5
                      u=u0*cs+c5/c6*(u0*w0*cdelta-v0*sdelta)
                      v=v0*cs+c5/c6*(v0*w0*cdelta+u0*sdelta)
                      w=w0*cs-c5*c6*cdelta
         endif
      return
      end
c*****************************************************************
       subroutine location(x,y,z,u,v,w,e,mat,ip,Npmax)
c      this subroutine calculates the new x,y,z locations
       implicit double precision (a-h,o-z)
       dimension x(Npmax),y(Npmax),z(Npmax)
       common/rand/grand

          call attent(e,mat,sigt)
          if(mat.eq.2)dens=1.0
          if(mat.eq.1)dens=1.2
          r1=ran3(grand)

          dl=-1.0*log(r1)/(sigt*dens)
          x(ip)=x(ip)+u*dl/2.54
          y(ip)=y(ip)+v*dl/2.54
          z(ip)=z(ip)+w*dl/2.54
        return
       end
c****************************************************************
      subroutine attent(e,mat,sigt)
c****subroutine that returns the attenuation coeffecient of the
c*****material
      implicit double precision(a-h,o-z)
      dimension mf(4),nsif(4),mcif(4),gadf(4)
      double precision mf,nsif,mcif,gadf
      data mf/ 1125.6,836,-147.4121,590/
      data nsif/0.2116,-16.63003,661.72,555.6709/
      data mcif/0.853577e-01,-0.230837,707,70252.4/
      data gadf/0.590663e-01,11.3653, 213.699,31842.5/
       sigm=0.0
       sigsn=0.0
       sigsm=0.0
       sigsg=0.0
       do i=1,4
           if(mat.eq.1)then
           sigm=sigm+mf(i)/e**(i-1)
           sigt=sigm
            elseif(mat.eq.2)then
              sigsn=sigsn+nsif(i)/e**(i-1)
              sigt=sigsn
                elseif(mat.eq.3) then
                   sigsm=sigsm+mcif(i)/e**(i-1)
                   sigt=sigsm
                   elseif(mat.eq.4) then
                    sigsg=sigsg+gadf(i)/e**(i-1)
                    sigt=sigsg
                    else
                    endif
           enddo
       return
       end
c****************************************************************
      subroutine attens(e,mat,sigs)
c****subroutine cdat returns the attenuation coeffecient of the
```

```
c*****material
      implicit double precision(a-h,o-z)
      dimension mf(4),nalf(4),mclf(4),gadf(4)
      double precision mf,nalf,mclf,gadf
      data mf/-3.1E-3,0.816,-63.0933,3639.86/
      data nalf/0.8867,-0.9736,-39.59,20515.75/
      data mclf/0.853577e-01,-0.236837,787,79252.4/
      data gadf/0.580863e-01,11.3653,-213.808,31842.5/
       sigm=0.0
       sigmn=0.0
       sigcm=0.0
       sigsg=0.0

       do i=1,4
          if(mat.eq.1)then
          sigm=sigm+mf(i)/e**(i-1)
          sigs=sigm
           elseif(mat.eq.2)then
             sigmn=sigmn+nalf(i)/e**(i-1)
             sigs=sigmn
               elseif(mat.eq.3) then
                 sigcm=sigcm+mclf(i)/e**(i-1)
                 sigs=sigcm
                 elseif(mat.eq.4) then
                  sigsg=sigsg+gadf(i)/e**(i-1)
                  sigs=sigsg
                  else
                  endif
          enddo
       return
       end
c*******************************************************************
c*****************************************************************
      subroutine attena(e,mat,sigs)
c****subroutine that returns the attenuation coeffecient of the
c*****material
      implicit double precision(a-h,o-z)
      dimension mf(4),nalf(4),mclf(4),gadf(4)
      double precision mf,nalf,mclf,gadf
      data mf/0.11569,5.07747,-83.4975,451.60586/
      data nalf/0.867280,5.8747479,-80.4488,548.7633/
      data mclf/0.853577e-01,-0.236837,787,79252.4/
      data gadf/0.590063e-01,11.3653,-213.909,31642.5/
       sigm=0.0
       sigmn=0.0
       sigcm=0.0
       sigsg=0.0

       do i=1,4
          if(mat.eq.1)then
          sigm=sigm+mf(i)/e**(i-1)
          sigs=sigm
           elseif(mat.eq.2)then
             sigmn=sigmn+nalf(i)/e**(i-1)
             sigs=sigmn
               elseif(mat.eq.3) then
                 sigcm=sigcm+mclf(i)/e**(i-1)
                 sigs=sigcm
                 elseif(mat.eq.4) then
                  sigsg=sigsg+gadf(i)/e**(i-1)
                  sigs=sigsg
                  else
                  endif
          enddo
       return
       end
```

```
c *****************************************************************
        subroutine position(x,y,z,mat,ip,npmax)
        implicit double precision(a-h,o-z)
        dimension x(Npmax),y(Npmax),z(Npmax)
c       mat=1 is the mine
c       mat=2 is soil
        common/locam/xm0,ym0,h,R,hl,zm0,cl
        tt=(x(ip)-xm0)**2+(y(ip)-ym0)**2
        cc=r**2
        zp=z(ip)-zm0

        hh=h+Hl
        if(tt.le.cc)then
                if((zp.ge.h).and.(zp.lt.hh))then
                  mat=1
                else
                  mat=2
                endif
        else
                 mat=2
        endif
        return
        end
c****************************************************************
       subroutine statout(x,y,z,ex,ey,mat,dep,Npmax,det,rl,sdet)
c A routine which returns the statistical values
       implicit double precision(a-h,o-z)
       dimension x(Npmax),y(Npmax),z(Npmax),mat(Npmax),dep(Npmax)
       dimension sx(npmax),sy(npmax)
          sdet=0.0
          si=0.0

        do ip=1,npmax
              if (dep(ip).gt.0.0) then
                        sdet=sdet+(det-dep(ip)/Npmax)**2
             else
             endif
        end do
          sdet=sdet**0.5/(npmax-1)
c

       return
       end

c*****************************************************************
       subroutine weight(mat,e,wei)
       implicit double precision(a-h,o-z)
                  call attenn(e,mat,sigs)
                  call attena(e,mat,sigm)

                  wei=wei*sigm/sigs
                  if(mat.eq.1)wei=wei*1.0
                  if(mat.eq.2)wei=wei*0.5
         return
         end
c****************************************************************

c*****************************************************************
       FUNCTION ran3(idum)
C      Taken from Numerical Recipes
       implicit double precision(a-h,o-z)
       double precision idum
c      this routine is from numerical recipes-by Press
c       INTEGER MBIG,MSEED,MZ
       double precision MBIG,MSEED,MZ
       DOUBLE PRECISION ran3,FAC
```

```
c      PARAMETER (MBIG=1000000000,MSEED=161803398,MZ=0,FAC=1.d0/MBIG)
       PARAMETER (MBIG=4000000.d0,MSEED=1618033.d0,MZ=0.d0,FAC=1.d0/MBIG)
       INTEGER i,iff,ii,inext,inextp,k
c      INTEGER mj,mk,ma(55)
       double precision mj,mk,ma(55)
       SAVE iff,inext,inextp,ma
       DATA iff /0/
       if(idum.lt.0.or.iff.eq.0)then
         iff=1
         mj=MSEED-abs(idum)
         mj=mod(mj,MBIG)
         ma(55)=mj
         mk=1
         do  i=1,54
           ii=mod(21*i,55)
           ma(ii)=mk
           mk=mj-mk
           if(mk.lt.MZ)mk=mk+MBIG
           mj=ma(ii)
          enddo
         do  k=1,4
           do  i=1,55
             ma(i)=ma(i)-ma(1+mod(i+30,55))
             if(ma(i).lt.MZ)ma(i)=ma(i)+MBIG
         enddo
        enddo
         inext=0
         inextp=31
         idum=1
       endif
       inext=inext+1
       if(inext.eq.56)inext=1
       inextp=inextp+1
       if(inextp.eq.56)inextp=1
       mj=ma(inext)-ma(inextp)
       if(mj.lt.MZ)mj=mj+MBIG
       ma(inext)=mj
       ran3=mj*FAC
       return
       end

        c*******************************************************************
```

LIST OF REFERENCES

1 Harding G, Kosanetzky J, "Status and outlook of coherent x-ray scatter imaging," J Optical Society of America, A4(5), 933-944 (1987).

2 Harding G, Kosanetzky J, "Scatter x-ray beam nondestructive testing," Nuclear Instrumentation and Methods in Physics Research, A280, 517-528 (1989)

3 Herr M D, McInerney J J, Lamser D G, Copenhaver G L, " A flying spot x-ray system for Compton backscatter imaging," IEEE transactions on Medical imaging, 13(3), 461-469 (1994).

4 Schönfelder V, Diehl R, Lichti G G, Steinle H, "The imaging Compton telescope COMTEL on the gamma ray observatory," IEEE Transactions on Nuclear Science, NS-31 (1), 766-770 (1984).

5 Anghaie S, Baker A G, Jacobs A M, Kondic N N, "Spatial distribution of phases in flow channels by analysis of Compton profile measurements" in Measurements in polyphase flows, Ed, Hendrick T R and Patel M R, ASME, New York, 13-17 (1982).

6 McInerney J J, Lamser D G, Herr M D, "A device for non-invasive evaluation of coronary bipass grafts," IEEE Transactions on Medical Imaging, 13(4), 659-665 (1994).

7 Campbell J G and Jacobs A M, "Detection of buried landmines by Compton backscatter imaging," Nuclear Science and Engineering, 110, 417-424 (1992).

8 Watanabe Y, Monroe J, Keshavmurthy S, Jacobs A M, Dugan E T, "Computational methods for shape restoration of buried objects in Compton backscatter imaging," Nuclear Science and Engineering, 122, 55-67 (1996).

9 Wehlburg J, Keshavmurthy S, Watanabe Y, Dugan E, Jacobs A, "Image restoration techniques using Compton backscatter imaging for detection of buried landmines," SPIE Proceedings on Detection Technologies for Mine and Minelike Targets, 2496, 336-347 (1995).

10 Keshavmurthy S P, Dugan E T, Wehlburg J C, Jacobs A M, "Analytical studies of a backscatter x-ray imaging landmine detection system," SPIE Proceedings on Detection Technologies for Mine and Minelike Targets, 2765-52 (1996).

11 Carter L L, and Cashwell E D, Particle transport simulation with Monte Carlo method, Technical Information Center, Office of Public Affairs, US Energy Research and Development Administration, Washington, DC (1975).

12 Blomquist R N, Gelbart E M, "An assessment of existing Klein-Nishina Monte-Carlo sampling methods," Nuclear Science and Engineering, 83, 380-384 (1983)

13 Briesmeister J F, Ed , "A general Monte-Carlo code for N-particle transport, version 4A," LA-12625-M, Los Alamos, NM (1993)

14 Hendricks J S, "Effects of changing the random number stride in Monte-Carlo calculations," Nuclear Science and Engineering, 109, 86-91 (1991)

15 West J T III, SABRINA: An interactive three-dimensional geometry-modeling program for MCNP, LA-10688-M, Los Alamos, NM(1986)

16 Cambell J G, Landmine detection by scatter radiation radiography, Ph D dissertation, University of Florida, Gainesville, FL (1997)

17 Dodson S L, Analytical calculations in support of research on a landmine detection system using backscattered x-rays, Masters project, Department of Nuclear Engineering Sciences, University of Florida, Gainesville, FL (1994)

18 Tucker D M, Barnes G T, Chakrraboty D P, "Semi-empirical model for generating tungsten target x-ray spectra," Medical Physics, 18(2), 211-218 (1991)

19 Tan D, Heaton B, "Bremsstrahlung intensity and spectrum-theoretical deduction and discussion," Applied Radiation and isotopes, 45(11), 1101-1111 (1994)

20 Press W, Teukolsky S A, Vetterling W T, Flannery B F, Numerical recipes in Fortran- The art of scientific computing, Second edition -Cambridge University press, New York, (1992)

21 Berger M J, Hubble J H, XCOM: Photon cross-sections on a personal computer, NBSIR 87-3597, US Department of Commerce, Gaithersburg, MD (1990)

22 Laine A F, Schuler S, Fan J, and Huda W, " Mammographic feature enhancement by multiscale analysis," IEEE transactions on Medical Imaging, 13(4), 741-751 (1994)

23 Mallat S G, "A theory for multi resolution signal decomposition: The wavelet representation," IEEE Transactions on Pattern Analysis and Machine Intelligence, 11(7), 674-693 (1989)

24 Mallat S and Zhong S,"Characterization of signals for multi-scale edges," IEEE transactions on PAMI, 14(7), 710-732 (1992).

25 Daubechies I, "The wavelet transform, time-frequency localization and signal analysis," IEEE transactions on Information Theory, 36 (5), 961-1005 (1990),

26 Benedetto J J, "Frame decompositions, sampling, and uncertainty principle" in Wavelets Mathematics and Applications, Ed ., Benedetto J J and Frazier M W, 247 -353, (1994)

27 Saito N, *Local feature extraction and its application using Library of Bases*, Ph.D. dissertation, Yale University, New Haven, December 1994.

28 Unser M, Aldroubi A, Eden M, "Fast B-spline transforms for continuous image representation and interpolation," IEEE Transactions on PAMI, 13 (3), 277-294 (1991)

29 Pentland A P, "Interpolation using wavelets," IEEE Transactions on PAMI, 16(4), 410-414 (1994)

30 Hanselman D, Littlefield B, *The MATLAB Version 4.0 User's guide, Mathworks Inc*, Prentice-Hall, Englewood Cliffs, NJ, 1995

31 Ashley S, "Searching for landmines," Mechanical Engineering, 118(4), 62-67 (1996)

32 Halbleib J A, Mehlhorn T A, "ITS: The integrated TIGER series of coupled electron/photon Monte Carlo transport codes," RSIC computer code collection, CCC-467, Sandia National Laboratories, Albuquerque, NM (1984)

BIOGRAPHICAL SKETCH

Shyam P. Keshavmurthy is from Bangalore, India and obtained his bachelors degree in mechanical engineering from the University of Mysore, India in 1987. He worked as a trainee reactor operations and maintenance engineer at Bhabha Atomic Research Center, Bombay, India from 1987-1988 and as a fuel design engineer at the Nuclear Power Corporation of India, Ltd., from 1988-1992. He obtained his master's degree in nuclear engineering from the University of Florida in December 1993 and will be completing his Ph D in nuclear engineering in August of 1996. He will be joining the Department of Radiology at the University of Michigan, Ann Arbor to pursue an academic career.

I certify that I have read this study and that in my opinion it conforms to acceptable standards of scholarly presentation and is fully adequate, in scope and quality, as a dissertation for the degree of Doctor of Philosophy.

Edward T Dugan

Edward T. Dugan, Chair
Associate Professor of
Nuclear Engineering Sciences

I certify that I have read this study and that in my opinion it conforms to acceptable standards of scholarly presentation and is fully adequate, in scope and quality, as a dissertation for the degree of Doctor of Philosophy

Alan M Jacobs

Alan M. Jacobs, Professor of
Nuclear Engineering Sciences

I certify that I have read this study and that in my opinion it conforms to acceptable standards of scholarly presentation and is fully adequate, in scope and quality, as a dissertation for the degree of Doctor of Philosophy

Nils J. Diaz, Professor of
Nuclear Engineering Sciences

I certify that I have read this study and that in my opinion it conforms to acceptable standards of scholarly presentation and is fully adequate, in scope and quality, as a dissertation for the degree of Doctor of Philosophy

Andrew F. Laine

Andrew F. Laine
Associate Professor of
Computer and Information Science
and Engineering

I certify that I have read this study and that in my opinion it conforms to acceptable standards of scholarly presentation and is fully adequate, in scope and quality, as a dissertation for the degree of Doctor of Philosophy.

Joseph Glover

Joseph Glover
Professor of Mathematics

This dissertation was submitted to the Graduate Faculty of the College of Engineering and to the Graduate School and was accepted as partial fulfillment of the requirements for the degree of Doctor of Philosophy

August, 1996

Winfred M. Phillips
Dean, College of Engineering

Karen A. Holbrook
Dean, Graduate School